

DENSITY CONTROLLED PHOTON PAIR GENERATION:
A PROTOTYPE SOURCE OF TUNABLE
ENTANGLED PHOTONS FROM
SUPERCritical XENON

by

KYLE EDWARD KLARUP

A DISSERTATION

Presented to the Department of Physics
and the Graduate School of the University of Oregon
in partial fulfillment of the requirements
for the degree of
Doctor of Philosophy

September 2017

DISSERTATION APPROVAL PAGE

Student: Kyle Edward Klarup

Title: Density Controlled Photon Pair Generation: a Prototype Source of Tunable Entangled Photons from Supercritical Xenon

This dissertation has been accepted and approved in partial fulfillment of the requirements for the Doctor of Philosophy degree in the Department of Physics by:

Daniel Steck	Chairperson
Michael Raymer	Advisor
Ben McMorran	Core Member
Jeffrey Cina	Institutional Representative

and

Sara D. Hodges	Interim Vice Provost and Dean of the Graduate School
----------------	--

Original approval signatures are on file with the University of Oregon Graduate School.

Degree awarded September 2017

© 2017 Kyle Edward Klarup

DISSERTATION ABSTRACT

Kyle Edward Klarup

Doctor of Philosophy

Department of Physics

September 2017

Title: Density Controlled Photon Pair Generation: a Prototype Source of Tunable Entangled Photons from Supercritical Xenon

This dissertation describes the development and verification of a fiber based prototype system for generating entangled photon pairs with a reduced spontaneous Raman scattering background compared to solid-core optical fibers. To achieve this goal, the guidance properties of hollow-core photonic bandgap fibers are combined with the density variability and high optical nonlinearity of supercritical xenon fluid. The dispersion properties of the system provide the proper conditions for the spontaneous generation of entangled photons by the nonlinear process of degenerate four-wave mixing. By altering the density of supercritical xenon in the fiber, the conditions for the four-wave mixing can be modified to tune the frequencies of the entangled photons.

CURRICULUM VITAE

NAME OF AUTHOR: Kyle Edward Klarup

GRADUATE AND UNDERGRADUATE SCHOOLS ATTENDED:

University of Oregon, Eugene
Grinnell College, Grinnell, Iowa

DEGREES AWARDED:

Doctor of Philosophy, Physics, 2017, University of Oregon
Master of Science, Physics, 2012, University of Oregon
Bachelor of Arts, Physics, 2010, Grinnell College
Bachelor of Arts, Religious Studies, 2010, Grinnell College

AREAS OF SPECIAL INTEREST:

Nonlinear Optical Physics

PROFESSIONAL EXPERIENCE:

Research assistant, Department of Physics, University of Oregon, Eugene 2010-
2017

GRANTS, AWARDS, AND HONORS:

Presidential Management Fellows Finalist, 2017

PUBLICATIONS:

Lynch-Klarup KE, Mondloch ED, Raymer MG, Arrestier D, Gerome F, Benabid F. Supercritical xenon-filled hollow-core photonic bandgap fiber. Optics Express. 2013;21(11):13726-32. doi: 10.1364/OE.21.013726.

ACKNOWLEDGMENTS

There are not enough words to properly convey the thanks, appreciation, and gratitude I owe to so many people for helping me get to this point, so instead let me spend just a few words on a few, but know you all have my deepest thanks.

To my advisor, Dr. Michael Raymer, for his constant tutelage and his boundless patience when yet another setback occurred in the lab. Your passion for physics and care you give to your students both amaze me, and I count myself among the fortunate few (23 by the count of champagne bottles in the lab) who were able to learn from you as graduate students.

To my committee members, professors Daniel Steck, Ben McMorrان, and Jeffrey Cina, whose feedback and suggestions forced me to consider new ideas and have resulted in a stronger finished product.

To my labmates: Dileep Reddy, Dr. Erin Mondloch, Dr. Dash Vitullo, and Dr. Roger Smith, for countless conversations on physics, optics, careers, and life. When 5 people occupy the same rooms for many years and grow closer, that is a special thing.

To professors Fetah Benabid and Rodrigo Amezcua Correa, for graciously providing the fibers used through this work.

To professor John Hardwick, whose early suggestions and collaboration helped shape the direction and focus of this project.

To Dr. Jonathan Lavoie, whose late suggestions and collaboration helped finalize and finish this project.

To Amy Lynch, Doug Klarup, and Erin Lynch-Klarup, for patiently supporting the family member who still, still is in school.

And finally, to my wife Amy Klarup, who fell in love with this silly physicist and has filled my life with music and joy.

TABLE OF CONTENTS

Chapter	Page
I. INTRODUCTION.....	1
1.1. Photon Pairs	1
1.2. Photon Pair Sources	3
1.3. Outline.....	4
II. MATHEMATICAL DESCRIPTION OF LIGHT	7
2.1. Light as a Field.....	8
2.2. Linear Solution to the Wave Equation.....	9
2.3. First-Order Interference, $g^{(1)}$	11
2.4. Mach-Zehnder Interferometer.....	12
2.5. Second-Order Interference, $g^{(2)}$	14
2.6. Classical Nonlinear Wave Equation	16
2.7. Quantizing the Electromagnetic Field	21
2.8. Quantum $g^{(2)}$	22

Chapter	Page
2.9. Quantum Picture of Degenerate FWM	24
III. Hollow-Core Optical Fibers.....	27
3.1. Brief Overview of TIR.....	28
3.2. Photonic Crystal and Bragg Scattering	29
3.3. Altering the Guidance Window by Changing Refractive Index	32
3.4. Dispersion of Light in the Guidance Window	33
3.5. Birefringence.....	36
3.6. Surface Modes	37
IV. XENON	38
4.1. Ideal Filling Fluid	39
4.2. Raman Scattering.....	40
4.3. Noble Properties.....	41

Chapter	Page
V. PROTOTYPE DESIGN.....	47
5.1. Xenon Containment System	47
5.2. Fiber Cells.....	49
5.3. Filling the Fiber.....	53
VI. TUNING GUIDANCE WINDOW WITH SUPERCRITICAL XENON	55
6.1. Experimental Setup.....	56
6.2. Measuring Guidance Window Edge	57
6.3. Comparing to Theoretical Model.....	60
VII. TUNING DISPERSION PROFILE WITH SUPERCRITICAL XENON	62
7.1. Experimental Setup.....	62
7.2. Measuring Group Velocity and GVD	64
7.3. Birefringence.....	66
7.4. Dispersion Pressure Dependence.....	67

Chapter	Page
VIII. MODEL FOR DISPERSION IN FLUID FILLED FIBER	69
8.1. Modeling Phase Refractive Index	70
8.2. Dispersion Pressure Dependence	72
8.3. More Work to be Done	77
XI. ENTANGLED PHOTON GENERATION BY FOUR-WAVE MIXING.....	78
9.1. Experimental Setup.....	78
9.2. Observations of Sidebands.....	79
9.3. Energy Conservation.....	81
9.4. Seeding.....	84
9.5. Single Photon Statistics Setup	85
9.6. Correlations vs Delay.....	87
9.7. Calculating the Accidental Coincidences	88
9.8. Second-Order Correlations	91

Chapter	Page
X. CONCLUDING REMARKS.....	95
REFERENCES CITED.....	100

LIST OF FIGURES

Figure	Page
2.1. Diagram of Mach-Zehnder interferometer.....	13
2.2. Diagram of a 2 nd -order correlation measurement.	15
2.3. Diagram of heralded 2 nd -order correlation measurement.	23
3.1. TIR in solid fiber.....	28
3.2. 1D Bragg scattering	30
3.3. 1D photonic crystal	30
3.4. HC-PBG fiber face.....	32
3.5. Phase matching solutions to four-wave mixing.....	36
4.1. Phase diagram of xenon	43
4.2. Xenon density equation of state.....	44
4.3. Xenon phase refractive index.....	45
5.1. Xenon containment system	48
5.2. Short fiber cell.....	50
5.3. Long fiber cell.....	52
6.1. Guidance window experimental setup.....	57
6.2. Guidance window spectrum vs pressure.....	58
6.3. Guidance window edge vs theory	60
7.1. Experimental setup: group velocity	63
7.2. Group velocity measurements.....	65
7.3. Birefringence in group velocity	66

Figure	Page
7.4. Group velocity vs pressure.....	67
8.1. Predicted phase matching curves	71
8.2. Quadratic fit to Sellmeier.....	73
8.3. Group and phase refractive index in toy model	74
8.4. Combined group refractive index at 1 atm	75
8.5. Combined group refractive index at 70 atm	76
9.1. Sideband experimental setup	79
9.2. Sideband pump peak power dependence	80
9.3. Observed birefringence and energy conservation.....	82
9.4. Comparing measured sideband wavelengths to predictions	84
9.5. Seeded amplification.....	85
9.6. Correlations setup	86
9.7. Coincidence as a function of delay	88
9.8. Quadratic coincidence with power.....	91
9.9. Experimental setup for 2 nd -order correlation	92

LIST OF TABLES

Table	Page
3.1. Nonlinear polarizability of noble gases	42
9.1. FPGA recordings for 2 nd -order correlation	93

CHAPTER I

INTRODUCTION

The generation and manipulation of specific quantum states of light is increasingly important in a range of quantum optical technologies, including developing quantum computers that can perform certain tasks more efficiently than classical computers [1], providing completely secure communication [2], and enhancing the ability to use light as for sensing and metrology [3, 4]. This is in part because photons, the ubiquitous term for the quantum of electromagnetic radiation [5], are an attractive vehicle for creating and transmitting quantum information over long distances because they are relatively easy to generate, travel at the speed of light, interact weakly with their environment, and can be manipulate with linear optics [6].

However, challenges still exist. This dissertation describes efforts to develop a system to address some of those challenges by developing a prototype system capable of generating correlated, entangled photons at tunable frequencies and frequency separations. Such a system shows promise at expanding the limits and possibilities of generating quantum states of light.

1.1 Photon Pairs

One particular use of photon pairs is as a source for single photons, which in turn are used in quantum information processing [7, 8]. It is difficult to generate single photons [9], and it is even harder to generate single photons deterministically [6]. And

definitively checking to see if a photon has been generated has the unfortunate side effect of annihilating the photon.

Photon pairs provide a solution to the problem of verifying the existence of a single photon. The measurements and annihilation of one of the photons in the pair can be used to herald the existence of the other photon. The effectiveness of such systems to herald the existence of a single photon is directly dependent on the correlation between the existence of the measured photon and the existence of the heralded photon. If a system that generates photon pairs also produces single photons with similar characteristics to the photons in the generated pair, the correlation is decreased and effectiveness is lost [6].

A common source of such uncorrelated photons is Raman scattering [10, 11], the process where energy is transferred to or from the vibrational modes of the material, shifting the light's frequency [12]. Reducing or removing such sources of uncorrelated photons can improve the effectiveness of photon pair generation as a source of heralded single photons.

Systems that can produce photon pairs are also capable of translating the quantum information from a photon at one frequency to a photon at another frequency [13]. These systems may be used to facilitate communication between quantum systems that operate at different optical frequencies. Again, sources of light outside of the degrees of freedom used to generate the photon at the new frequency add noise and errors to the process.

1.2 Photon Pair Sources

Crystals can generate photon pairs through a down-conversion process where a single, high-energy photon is annihilated and two lower-energy photons are created. Crystals are simple to put into experimental systems, and the frequencies of the photons generated can be tuned, to an extent, by rotating the crystal [6]. However, the frequency of the high-energy photon is limited by the crystal's structure and the lower-energy photons are produced in multi-mode cones along different propagation paths [6].

The generation of photon pairs in silica fiber addresses some of these limitations. The waveguide nature of the fiber results in the generated photon pairs co-propagating, making them easier to couple through additional optical systems. Long interaction lengths also provide for an enhancement of the linear features of the fiber and control over the state of the produced light by modifying the length of the fiber [14]. However, because the light is traveling through a large amount of silica, Raman scattering can lead to the creation of uncorrelated photons that are similar in frequency and time to the photon pairs [6]. Additionally, the parameters of fibers necessary to achieve the generation of photon pairs from a single pump limits the wavelengths available to the fibers to the near infrared and infrared wavelengths. The development of photonic crystals will be described in greater detail in Chapter 3, but it should be noted that the inclusion of a photonic crystal surrounding the solid silica core of a solid-core fiber made manufacturing of fibers that produced entangled photons at shorter wavelengths possible [15]. However, the issue of Raman scattering still persists.

To truly address the issue of Raman scattering, we can turn to fiber that guides light in a hollow core [16]. These cores could then be filled with fluids that had only very

weak vibrational modes [17-21] or discrete vibrational modes [22-24]. There are two main types of hollow-core fiber. The photonic bandgap fiber will be discussed in greater detail in Chapter 3, and is the fiber of choice for this dissertation. The other option is the Kagome fiber [25], which is believed to guide light through an ‘anti-resonant reflection optical waveguiding’ [26]. These fibers allow for the guidance of a broad range of wavelengths, but have only weak dispersion properties. As such, the dispersion of the filling fluid dominates when determining the wavelengths of generated photon pairs, which in turn limits them to being used with lower pressures of fluid.

This dissertation looks at how the properties of the hollow-core photonic bandgap (HC-PBG) fiber may be combined with those of supercritical xenon fluid to produce a system capable of addressing some of the limitations described in the above fiber systems.

1.3 Outline

Chapters 2-4 provide an overview of the various optical properties, technologies, and materials used to create a system capable of producing a fiber based system for tunable entangled photon pairs. The first chapter begins with a discussion of the essential properties and mathematical descriptions of light necessary for the work presented in the dissertation. From the foundational equations of classical light, it develops the wave equation for the propagating fields of electromagnetic radiation and looks at how the fields can interact in constructive and destructive ways based on their wave-like attributes. Both linear and nonlinear optics are explored, including the nonlinear theory of four-wave mixing, which describes the process used to generate entangled photon

pairs in this dissertation. Quantizing the electric field and the development of the analogous quantum equations for light is also discussed, as the generation of entangled photons is intrinsically quantum in nature.

Chapter 3 focuses on the properties of hollow-core photonic crystal fiber waveguides necessary for the generation of tunable entangled photons. It begins with an intuitive description of photonic crystals and how they have been harnessed to create fibers capable of guiding light in a hollow core. Following sections discuss the ramifications of this guidance mechanism on the optical properties of the waveguide, from the wavelengths of light which can be confined to the dispersion profile of the waveguide, to how those properties may be altered by the inclusion of fluids into the system.

Chapter 4 is dedicated to the central material of this dissertation: xenon. It describes the properties which make it so appealing for this work. In particular, the fact that xenon is a noble gas with a relatively high optical nonlinear response and transitions from a gaseous state to a supercritical fluid at reasonable pressures and temperatures.

The development and design of experimental apparatuses needed to construct the prototype source of entangled photons are covered in Chapter 5. Xenon is a rare gas, and efforts had to be made to confine and recycle it over many experiments. This section highlights the systems that were created to allow the xenon to be brought to supercritical pressures, how to fill the fiber with xenon in a controllable and reversible manner, and how to be able to optically couple to the waveguide after being filled with xenon.

Experimental designs and results are presented in Chapters 6-9. The first experiments deal with the linear interaction of the light with the xenon filled fiber,

showing how the pressure of xenon in the fiber alters the guided wavelengths and dispersion profile of the system. A scalar model, originally developed in [27] is shown to hold at the densities of xenon used in this study, and that model is extended and modified to explain the way the dispersion profile of the fiber depends on the xenon density as well.

The last experimental chapter, Chapter 9, is dedicated to the production and measurement of correlated photons. Initial measurements with an interferometer are followed by detections of single photons and counting coincidences and correlations to verify the generation of non-classical light.

Finally, Chapter 10 provides some concluding remarks on the work presented and on future avenues that could be pursued.

CHAPTER II

MATHEMATICAL DESCRIPTION OF LIGHT

Creating, detecting, and verifying entangled photon pairs requires understanding how light interacts with matter and interferes with itself from both classical and quantum perspectives. This chapter provides an overview of the mathematical framework the prototype source of tunable entangled photon pairs is built upon. While the chapter does not try to replicate the breadth or completeness found in optical physics textbooks (see [5, 12, 28, 29] as good examples of such texts), it does attempt to provide a foundation to understand both the physical phenomena of entangled photon pair generation from degenerate four wave mixing and the methods used to validate said generation.

This chapter begins from the classical perspective of light as a field. From Maxwell's equations, a wave equation for describing the propagation and interaction of light with matter is developed. Key descriptors of light are drawn from the linear solution to that wave equation, and the effects of first and second order correlations between light fields discussed. The classical view of light concludes with solutions to the nonlinear wave equation that result in the generation of new frequencies of light from degenerate four-wave mixing (FWM).

This chapter then switches to a quantum perspective of light, focused on the local excitations of the electromagnetic field coined photons. The concept of quantizing the field is addressed, and the operators and states of quantum optics developed. The quantum version of second-order correlations is discussed and finally the generation of entangled photon pairs from the quantum view is performed.

2.1 Light as a Field

A classical perspective of light may be built around the idea of representing light as a field. For this view, light's propagation and interaction with matter can be described through the development of a wave equation. The foundations of this perspective are Maxwell's Equations,

$$\nabla \cdot \mathbf{D} = \rho \quad (2-1)$$

$$\nabla \cdot \mathbf{B} = 0 \quad (2-2)$$

$$\nabla \times \mathbf{E} = \frac{-\partial \mathbf{B}}{\partial t} \quad (2-3)$$

$$\nabla \times \mathbf{H} = \frac{\partial \mathbf{D}}{\partial t} + \mathbf{J}, \quad (2-4)$$

where \mathbf{E} is the electric field vector, \mathbf{H} is the magnetic field vector, \mathbf{D} is the electric flux density, \mathbf{B} is the magnetic flux density, ρ is the free charge density, and \mathbf{J} is the free current. When the electric and magnetic fields are traveling through a material, the fields may interact with the atoms, potentially inducing electric and magnetic polarizations (\mathbf{P} and \mathbf{M} , respectively) that modify the flux densities,

$$\mathbf{D} = \epsilon_0 \mathbf{E} + \mathbf{P} \quad (2-5)$$

$$\mathbf{B} = \mu_0 \mathbf{H} + \mathbf{M}, \quad (2-6)$$

where ϵ_0 and μ_0 are the vacuum permittivity and permeability.

In the materials discussed in this dissertation, several valid approximations may be made to simplify Maxwell's Equations and lead to a wave equation describing the propagation of the electric field. The materials used in this work are nonmagnetic, ($\mathbf{M} = 0$), devoid of free charges ($\rho = 0$), and have no free currents ($\mathbf{J} = 0$). With these assumptions, Maxwell's equations now take the form,

$$\nabla \cdot \mathbf{D} = 0 \quad (2-7)$$

$$\nabla \cdot \mathbf{B} = 0 \quad (2-8)$$

$$\nabla \times \mathbf{E} = \frac{-\partial \mathbf{B}}{\partial t} \quad (2-9)$$

$$\nabla \times \mathbf{B} = \mu_0 \frac{\partial \mathbf{D}}{\partial t}. \quad (2-10)$$

Taking the curl of Equation 2-9, inserting Equation 2-10 and making use of Equation 2-7, the wave equation for the electric field may be found:

$$\nabla^2 \mathbf{E} - \frac{1}{\epsilon_0 c^2} \frac{\partial^2}{\partial t^2} \mathbf{D} = 0. \quad (2-11)$$

Here the speed of light is defined as: $c = \sqrt{\frac{1}{\mu_0 \epsilon_0}}$.

2.2 Linear Solution to the Wave Equation

The electric flux density contains terms for the electric field and the induced polarization of the material. To get a wave equation purely in terms of the electric field, the induced polarization needs to be written in terms of \mathbf{E} . For relatively weak electric fields, the induced polarization may be accurately approximated as a linear response to the electric field, where the strength of the response is set by the linear susceptibility, $\chi^{(1)}$, of the material to being polarized by the field,

$$\mathbf{P} = \epsilon_0 \chi^{(1)} \mathbf{E}. \quad (2-12)$$

Returning to Equation 2-5, the electric flux may be written as

$$\mathbf{D} = \epsilon_0 (1 + \chi^{(1)}) \mathbf{E} = \epsilon_0 n^2 \mathbf{E}, \quad (2-13)$$

where

$$n = \sqrt{1 + \chi^{(1)}} \quad (2-14)$$

is the linear refractive index of the material defined in terms of the linear susceptibility.

Finally, the linear wave equation becomes:

$$\nabla^2 \mathbf{E} - \frac{n^2}{c^2} \frac{\partial^2}{\partial t^2} \mathbf{E} = 0,$$

where we see the speed of light in the material is set by the strength of the linear refractive index:

$$v = c/n. \quad (2-15)$$

Solutions to the wave equation take the form of plane waves:

$$\mathbf{E}(\mathbf{r}, t) = A_0 e^{i(\mathbf{k}\cdot\mathbf{r} - \omega t)}, \quad (2-16)$$

where A_0 is the amplitude of the field, ω is the frequency of the light, and \mathbf{k} the wave vector

$$\mathbf{k} = \frac{n(\omega)\omega}{c} \hat{\mathbf{r}}, \quad (2-17)$$

where \mathbf{k} may be found by solving the wave equation, and I have explicitly included the frequency dependence of the linear refractive index, $n(\omega)$. While the infinite extent of plane waves makes them unrealistic by definition, real modes of light may be represented by the superposition of plane waves [28]. In addition, optical fields may often be approximated as plane waves to gain insight into how the light will behave in the system.

The plane wave description of the electric field contains terms representing observables of the field. The energy of the field is encoded in the amplitude, A_0 , and observed in measurements of the optical intensity of the light:

$$I(\mathbf{r}, t) = |\mathbf{E}(\mathbf{r}, t)|^2. \quad (2-18)$$

The oscillations of the field are described either by the frequency (ω), wave vector (\mathbf{k}), or wavelength (λ), or the light, where

$$\lambda = \frac{1}{|\mathbf{k}|} = \frac{2\pi c}{n(\omega)\omega}, \quad (2-19)$$

and the wavelength depends on the refractive index of the material the light is propagating through.

2.3 First-Order Correlations, $g^{(1)}$

With a foundation of the wave equation and plane wave solutions built, observed interactions between different fields of light may be discussed. For example, consider the intersection of two plane waves with equal amplitudes but different frequencies at a particular point in space and time:

$$\mathbf{E}_1(\mathbf{r}, t) + \mathbf{E}_2(\mathbf{r}, t) = A_1 e^{i(\mathbf{k}_1 \cdot \mathbf{r} - \omega_1 t)} + A_1 e^{i(\mathbf{k}_2 \cdot \mathbf{r} - \omega_2 t)}. \quad (2-20)$$

The instantaneous intensity of such a combination of fields would then depend on a quickly oscillating term:

$$I(\mathbf{r}, t) = A_1^2 (2 + 2\cos[(\mathbf{k}_1 - \mathbf{k}_2) \cdot \mathbf{r} + (\omega_1 - \omega_2)t]) \quad (2-21)$$

Actual measurements of the intensity will be done over some amount of time, so the measured intensity is a time average of Equation 2-21:

$$\langle I \rangle = \int_0^T I(t) dt = 2A_1^2. \quad (2-22)$$

If, however, the frequencies of the two fields are the same, then Equation 2-20 reduces further to

$$\mathbf{E}_1(\mathbf{r}, t) + \mathbf{E}_2(\mathbf{r}, t + \tau) = 2A_1 e^{i(\mathbf{k}_1 \cdot \mathbf{r})} e^{-i\omega t} e^{-i\omega \tau}, \quad (2-23)$$

where I've rewritten the time component in terms of the delay between the 2 fields. Such a system has an intensity of

$$I = 2A_1^2(1 + \cos(\omega\tau)), \quad (2-24)$$

which is constant as long as the delay between the fields, τ , stays constant. Then the average intensity will depend on the particular value of τ but can range in value from 0 to $4A_1^2$.

When the observed intensity is high, the fields are said to constructively interfere and when the intensity is low, the fields are said to destructively interfere. The observation of the phenomena can be used to probe how light interacts with material.

The amount of interference between the two fields may be quantified as 1st-order interference, $g^{(1)}(\tau)$, defined as [5],

$$g^{(1)}(\tau) = \frac{\langle E^*(t)E(t + \tau) \rangle}{[\langle |E(t)|^2 \rangle \langle |E(t + \tau)|^2 \rangle]^{1/2}}, \quad (2-25)$$

where we have stopped explicitly labeling for the position and * indicates taking the complex conjugate of the field. It can be seen that $0 \leq g^{(1)}(\tau) \leq 1$.

2.4 Mach-Zehnder Interferometer

Interferometers such as the Mach-Zehnder exploit this interference in the amplitudes of two waves in order to measure properties of the light passage through a material within the spectrometer. The basic design of Mach-Zehnder interferometer is shown in Figure 2.1, where an incoming beam of light (E_0) is split by a beamsplitter and sent along the reference (E_1) and sample (E_2) arms of the interferometer. The reference arm generally has some method to controllably change its length, allowing the effective

optical path length of that arm to vary. The light is then recombined on a second beamsplitter and leaves the interferometer from two ports (E_3 and E_4). When the light is recombined on a second beamsplitter, the changes in the optical path length manifest in changing the value of the delay term, τ , in Equation 2-25.

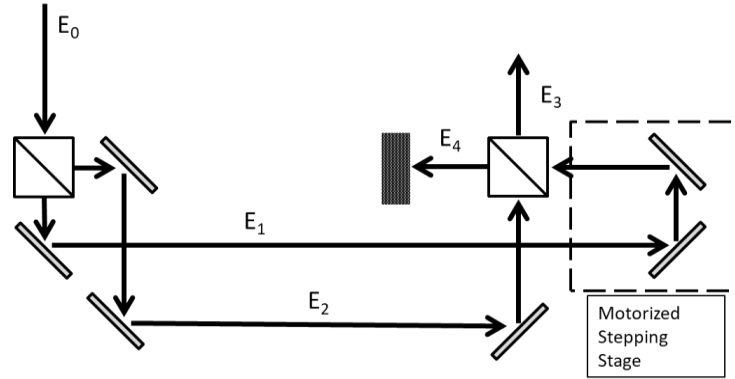


Figure 2.1. Diagram of a Mach-Zehnder Interferometer: The constructive or destructive interference of the optical fields from the two arms of the detector depend on the relative time delay set by the effective optical path lengths of each arm and the coherence length of the source light.

For continuous wave (CW) plane waves, this interference is cyclical, where delaying one wave with respect to the other allows the interference pattern to repeat indefinitely, i.e.,

$$g^{(1)}(\tau) = e^{-i\omega\tau}, \quad (2-26)$$

such that for $i\omega\tau = 0, \pi, 2\pi, \dots$

$$g^{(1)}(\tau) = 1, \quad (2-27)$$

and when $\omega\tau = \pi/2, 3\pi/2, \dots$

$$g^{(1)}(\tau) = 0. \quad (2-28)$$

In real systems, limitations on the bandwidth of the light, the consistency of the source and the pulse length of the field all cause this coherent interference to diminish with

increased delays and set a coherence time, τ_c , or time beyond which the interference effects will diminish and eventually disappear.

When operating with a non-ideal light source, the coherence time of the light will create an envelope over the periodic interference pattern. Maximum visibility will be observed at $\tau = 0$ and the $g^{(1)}(\tau)$ value will gradually diminish for increased delay times. For the purposes of the work presented in this dissertation, the Mach-Zehnder interferometer will be a useful tool for measuring the speed of light in a sample placed in one of the arms of the system.

Using a source with a very short coherence length, observing 1st-order coherence will only occur when $\tau \approx 0$. To determine the length of the reference arm that corresponds with $\tau = 0$, the visibility of observed fringes within the coherence length may be quantified as,

$$\text{visibility} = \frac{I_{\max} - I_{\min}}{I_{\max} + I_{\min}}. \quad (2-29)$$

With the maximum visibility in the fringe pattern observed when $\tau = 0$.

2.5 Second-Order Coherence, $g^{(2)}$

While the 1st-order correlation function, $g^{(1)}$, looked at correlations in the amplitudes of the electric fields, the 2nd-order correlation function, $g^{(2)}$, quantifies the intensity correlations between the fields. In a similar fashion to $g^{(1)}$, a general definition of $g^{(2)}$ for classical light may be written as [5],

$$g^{(2)}(r_1, t_1; r_2, t_2) = \frac{\langle I_1(r_1, t_1)I_2(r_2, t_2) \rangle}{\langle I_1(r_1, t_1) \rangle \langle I_2(r_2, t_2) \rangle}, \quad (2-30)$$

where r and t are the space-time locations of measurement, I is the intensity of the field at those locations, and $\langle \ \rangle$ indicates a time average.

the values of $g^{(2)}$ are limited to the range [5],

$$1 \leq g^{(2)} \leq \infty. \quad (2-31)$$

Experimentally observing $g^{(2)}$ relies on measuring the intensities of the separate fields. In this work, that will be accomplished by measuring the intensities of the fields at two different locations and observing how $g^{(2)}$ varies for different time delays. A typical measurement might be as shown in Figure 2.2, where the 2nd-order correlations of a single optical beam are measured by splitting the beam with a beamsplitter and measuring the intensities correlations of light along the two paths [30].

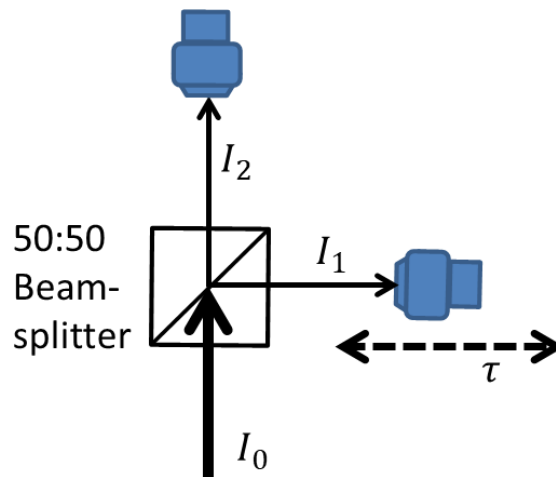


Figure 2.2. Diagram of a 2nd-Order Correlation Measurement: a simple cartoon of how a $g^{(2)}(\tau)$ measurement could be performed on a single field with optical intensity I_0 where the time delay, τ , between detections is set by the location of the detector long path 1.

In a scenario like the one shown in Figure 2.2, we can simplify $g^{(2)}$ to:

$$g^{(2)}(\tau) = \frac{\langle I_1(0)I_2(\tau) \rangle}{\langle I_1(0) \rangle \langle I_2(\tau) \rangle}, \quad (2-32)$$

where $\tau = t_1 - t_2$ is the difference in time between two detections and the spatial locations r_1 and r_2 are accounted for by the subscripts on the intensities.

2.6 Classical Nonlinear Wave Equations

All the previous work assumed a linear induced polarizability response to the optical field, which was sufficient to describe the coherence measurements expected from interference between the amplitude and intensity terms of a classical field. At higher optical intensities, the induced polarization no longer depends linearly on the field. The resulting nonlinear contribution opens the possibility for interactions between multiple fields of different frequencies, mediated by the presence of the nonlinear material. This will eventually allow for the generation of entangled photons.

The induced polarization, \mathbf{P} , may be generalized as a power series to account for this nonlinear response to strong electric fields:

$$\mathbf{P} = \epsilon_0 (\chi^{(1)} \mathbf{E} + \chi^{(2)} \mathbf{E} \mathbf{E} + \chi^{(3)} \mathbf{E} \mathbf{E} \mathbf{E} + \dots), \quad (2-33)$$

where $\chi^{(j)}$ is the $j+1$ rank tensor describing the j^{th} order susceptibility.

In symmetric materials like glass or noble gases, the 2nd order nonlinear susceptibility, $\chi^{(2)}$, contribution to the nonlinear response is zero, and the leading nonlinear contribution comes from $\chi^{(3)}$ [12]. Truncating the expansion of the polarizability there,

$$\begin{aligned}\mathbf{P} &= \epsilon_0\chi^{(1)}\mathbf{E} + \epsilon_0\chi^{(3)}\mathbf{E}\mathbf{E}\mathbf{E} \\ &= \mathbf{P}^{(1)} + \mathbf{P}^{(3)}.\end{aligned}\tag{2-34}$$

The electric flux density may be written in terms of the linear flux and the nonlinear correction term to the polarizability,

$$\begin{aligned}\mathbf{D} &= \epsilon_0\mathbf{E} + \epsilon_0\chi^{(1)}\mathbf{E} + \epsilon_0\chi^{(3)}\mathbf{E}\mathbf{E}\mathbf{E} \\ &= \mathbf{D}^{(1)} + \mathbf{P}^{(3)},\end{aligned}\tag{2-35}$$

and the wave equation can be rewritten with a nonlinear correction term:

$$\nabla^2\mathbf{E} - \frac{n(\omega)^2}{c^2}\frac{\partial^2}{\partial t^2}\mathbf{E} = \frac{1}{\epsilon_0c^2}\frac{\partial^2}{\partial t^2}\mathbf{P}^{(3)}.\tag{2-36}$$

Thanks to this nonlinear optical response, it is possible to generate new frequencies of light in the material by the process of degenerate four-wave mixing (FWM), which can be seen by solving the nonlinear wave Equation 2-36, as shown by Wang *et al.* in [12]. In degenerate FWM, a single CW pump frequency interacts with a material confined in a length of fiber and produces new light under the conditions of energy conservation,

$$2\omega_3 = \omega_1 + \omega_2,\tag{2-37}$$

and phase conservation,

$$2k_3 = k_1 + k_2,\tag{2-38}$$

where the subscripts indicating the pump (3) and sidebands (1,2) of the degenerate FWM process.

To see the importance of energy and phase conservation in a degenerate FWM scenario, let the total electric field comprise of three classical components [31]:

$$E(\mathbf{r}, t) = E_1(\mathbf{r}, t) + E_2(\mathbf{r}, t) + E_3(\mathbf{r}, t).\tag{2-39}$$

I will assume all three fields are overlapped and co-propagating in the same direction, z .

Then using separation of variables, field becomes:

$$E_j(r, t) = U_j(x, y)A_j(z)e^{ik_jz - \omega_j t} + c. c. \quad (2-40)$$

where the z -dependence is separated from the transverse dependence, loss is neglected, and “ $c. c.$ ” indicates the complex conjugate term.

Assuming the transverse components for each of the three modes are identical, solving the nonlinear wave equation for the combined field results in three equations for the amplitudes of each field:

$$\frac{dA_1(z)}{dz} = \frac{3i\omega_1^2\chi^{(3)}}{2k_1c^2} (2|A_3|^2A_1 + |A_3|^2A_2^* e^{i\theta}) \quad (2-41)$$

$$\frac{dA_2(z)}{dz} = \frac{3i\omega_2^2\chi^{(3)}}{2k_2c^2} (2|A_3|^2A_2 + |A_3|^2A_1^* e^{i\theta}) \quad (2-42)$$

$$\frac{dA_3(z)}{dz} = \frac{3i\omega_3^2\chi^{(3)}}{2k_3c^2} |A_3|^2A_3. \quad (2-43)$$

Here,

$$\theta = (2k_3 - k_1 - k_2)z - (2\omega_3 - \omega_1 - \omega_2)t, \quad (2-44)$$

and recall that,

$$k_j = \frac{n_j(\omega_j)\omega_j}{c}. \quad (2-45)$$

The equations for the amplitudes of the new sideband wavelengths (A_1 and A_2) are coupled. To uncover the evolution of the amplitudes as a function of z , Equation 2-45 may first be solved,

$$A_3(z) = A_3(0)e^{i\varphi(z)}, \quad (2-46)$$

with

$$\begin{aligned}\varphi(z) &= \frac{3\omega_3^2\chi^{(3)}}{2k_3c^2}|A_3|^2z \\ &= \gamma P_3z,\end{aligned}\tag{2-47}$$

where P_3 is the average pump power and γ is the nonlinear coefficient defined in terms of the nonlinear refractive index $n^{(2)}$, which itself is proportional to $\chi^{(3)}$,

$$\gamma = \frac{n^{(2)}\omega}{cA_{eff}}.\tag{2-48}$$

The second term in Equation 2-44 may be dropped due to energy conservation ($2\omega_3 - \omega_1 - \omega_2 = 0$), and the resulting coupled evolution equations for the amplitudes of the new frequencies may be written as

$$\frac{dA_1}{dz} = i\gamma(2P_3A_1 + P_3A_2^*e^{i(2\gamma P_3 - \Delta k)z})\tag{2-49}$$

$$\frac{dA_2^*}{dz} = -i\gamma(2P_3A_1e^{-i(2\gamma P_3 - \Delta k)z} + 2P_3A_2^*),\tag{2-50}$$

with

$$\Delta k = k_1 + k_2 - 2k_3\tag{2-51}$$

being the phase mismatch of the optical fields.

To solve these equations, new variables may be introduced to describe the amplitude evolution of the sideband of the degenerate FWM process,

$$B_j = A_j e^{-2i\gamma P_3 z}, (j = 1, 2)\tag{2-52}$$

yielding,

$$\frac{dB_1}{dz} = 2i\gamma P_3 B_2^* e^{-i(\Delta k + 2\gamma P_3)z} \quad (2-53)$$

$$\frac{dB_2^*}{dz} = -2i\gamma P_3 B_1 e^{i(\Delta k + 2\gamma P_3)z}. \quad (2-54)$$

Looking at these last 2 coupled equations, it becomes apparent why phase matching is a second required feature of generating meaningful signals from four wave mixing. Under most circumstances and for most frequencies of light, the term in the exponentials of Equations 2-53 and 2-54 may be substantial. This would cause the amplitudes of fields B_1 and B_2 to oscillate around very small values and never grow to a macroscopic value. Let me define this term as the phase matching of the system, κ , as

$$\begin{aligned} \kappa &= \Delta k + 2\gamma P_3 \\ &= k_1 + k_2 - 2k_3 + 2\gamma P_3. \end{aligned} \quad (2-55)$$

If, however, $\kappa \approx 0$, then this oscillation goes away and the amplitude of the light is free to grow to measurable values.

In the case of perfect phase matching, $\kappa = 0$, the gain of the system a distance z through the material can be found by comparing the field amplitude of 1 sideband at the start of the system to the strength of the field in the other sideband:

$$G = \left| \frac{B_1(z)}{B_2(0)} \right|^2 = |\gamma P_3 z|^2. \quad (2-56)$$

From this, we see that quadratic growth is expected for the gain of the intensity in the signal and idler frequencies when either the pump power is increased, the nonlinear coefficient increases, or the interaction distance z increases. This is only true under the assumption of a non-depleting pump (i.e. that P_3 stays constant throughout the length of the fiber).

Because this derivation has been done for classical fields, the gain when there are no initial fields B_1 and B_2 is ill-defined. A quantum view is needed in that case.

2.7 Quantizing the Electromagnetic Field

A full development of the quantum picture is put forth in [5], and stems from the idea that electromagnetic radiation is quantized. Thinking of these quanta as little particles of light termed photons is problematic [5]. Still, the term photon is so engrained in our way of discussing light that I will adopt it like everyone else has done.

Quantizing the electric field may be done by letting the fields be represented by operators and the addition or removal of quantized amounts of energy being carried out by creation and annihilation operators. These operators act on eigenstates of the electromagnetic field, called number states, $|n\rangle$, where n indicates the number of photons of a particular spatial mode of the state.

A single photon may be added or removed from a number state by means of creation and annihilation operators (\hat{a}^\dagger, \hat{a}) such that,

$$\hat{a}^\dagger |n\rangle = \sqrt{n+1} |n+1\rangle \quad (2-57)$$

$$\hat{a} |n\rangle = \sqrt{n} |n-1\rangle. \quad (2-58)$$

A photon number state with one photon may then be written in terms of a creation operator acting on the vacuum,

$$|1\rangle = \hat{a}^\dagger |vac\rangle. \quad (2-59)$$

The energy carried in a quanta of the electric field depends on the frequency of the field. To account for this in the number state representation of light, let me add a frequency dependence,

$$|1_\omega\rangle = \hat{a}^\dagger(\omega)|vac\rangle. \quad (2-60)$$

For classical fields, a realistic representation of light is built by superimposing many plane waves. The same thing must be done when quantizing that field. The result is that the photon state could cover a range of frequencies,

$$|1_\omega\rangle = \int d\omega_i f(\omega_i)\hat{a}^\dagger(\omega_i)|vac\rangle, \quad (2-61)$$

where $f(\omega_i)$ contains information about the frequency distribution or spectral amplitude function of the photon, where the single frequency, ω , in Equation 2-60 becomes the central frequency of the distribution.

2.8 Quantum $g^{(2)}$

With a quantized field, the 2nd-order correlation measurements will change.

Consider the event of a single photon entering a system like that shown in Figure 2.2. The detection of that photon by either detector annihilates the state, leaving only vacuum. So a photon should never be measured by both detectors simultaneously and $g^{(2)}$ should be zero—in violation of the inequality developed with classical fields and expressed in Equation 2-33. We can redefine $g^{(2)}$ for quantized light in a single mode as [5],

$$g^{(2)}(\tau) = \frac{\langle \hat{a}^\dagger \hat{a}^\dagger \hat{a} \hat{a} \rangle}{\langle \hat{a}^\dagger \hat{a} \rangle^2}, \quad (2-62)$$

where it can be shown the value of $g^{(2)}$ will depend on the number of photons being measured,

$$g^{(2)}(\tau) = 1 + \frac{\Delta n^2 - \langle n \rangle}{\langle n \rangle^2}. \quad (2-63)$$

This yields a different inequality,

$$1 - \frac{1}{\langle n \rangle} \leq g^{(2)}(\tau). \quad (2-64)$$

This inequality returns the expected prediction for a single photon in the system: it won't be detected by both detectors.

Experimentally, we can write the value of 2nd-order coherence based on the probability of detections by detectors as,

$$g^{(2)}(\tau) = \frac{P_{AB}}{P_A P_B} f,$$

where P_{AB} is the probability of detecting coincidences between both detectors, P_A and P_B are the probabilities for the individual detectors to detect a photon, and f defines the frequency that photons are introduced to the system.

A slightly modified design can remove the need to know the probabilities of the detectors and the frequency at which photons enter the system. If the photon entering the system is produced by a source along with another photon, the second photons may be used to herald the existence of the photon in the detection system as shown in Figure 2.3.

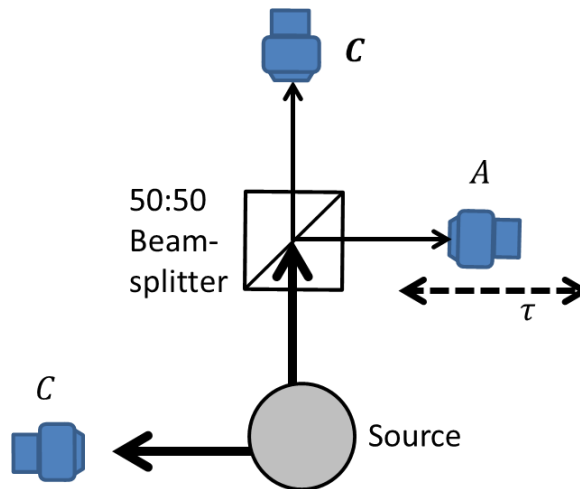


Figure 2.3. Diagram of a Heralded 2nd-Order Quantum Correlation Measurement: a cartoon of how a $g^{(2)}(\tau)$ measurement could be performed on a single photon from a pair of correlated photons.

With such a design, a heralded $g^{(2)}$ measurement may be performed where

$$g^{(2)}(\tau) = \frac{P_{ABC}P_C}{P_{AC}P_{BC}}, \quad (2-65)$$

or in terms of the counts from the detectors:

$$g^{(2)}(\tau) = \frac{N_{ABC}N_C}{N_{AC}N_{BC}}, \quad (2-66)$$

where different probabilities of detection between the detectors cancel from the numerator and denominator [32].

2.9 Quantum Picture of Degenerate FWM

In a quantum picture of degenerate FWM, two photons from the pump are annihilated to create a photon in the signal sideband and a photon in the idler sideband.

This state may be written as,

$$|\psi\rangle = T e^{-i \int_0^t dt' \hat{H}(t')} |\text{pump}\rangle \otimes |\text{vac}\rangle, \quad (2-67)$$

where T is the time-ordered operator and the Hamiltonian is defined as

$$\hat{H}(t) = \int_0^L dz \gamma \hat{E}_p^{(+)}(z, t) \hat{E}_p^{(+)}(z, t) \hat{E}_s^{(-)}(z, t) \hat{E}_i^{(-)}(z, t). \quad (2-68)$$

The state $|\psi\rangle$ can be used to find the state where 2 photons are generated by degenerate FWM by expanding the exponential around the vacuum state and keeping only the term related to the creation of two photons,

$$|\psi_2\rangle = -i\epsilon \int_{-\infty}^{\infty} dt' \hat{H}(t') |\text{pump}\rangle \otimes |\text{vac}\rangle. \quad (2-69)$$

Dropping normalizing terms yields,

$$\begin{aligned}
|\psi_2\rangle &= \int_{-\infty}^{\infty} dt' \int_0^L dz \gamma \widehat{E}^{(+)}(z, t) \\
&\int_0^{\infty} d\omega \widehat{a}_p e^{-i(k_p z - \omega_p t)} \int_0^{\infty} d\omega' \widehat{a}_p e^{-i(k_p z - \omega'_p t)} \\
&\int_0^{\infty} d\omega'' a_s^\dagger e^{i(k_s z - \omega''_s t)} \int_0^{\infty} d\omega''' a_i^\dagger e^{i(k_i z - \omega'''_i t)} |\text{pump}\rangle \otimes |\text{vac}\rangle.
\end{aligned} \tag{2-70}$$

Energy conservation appears from the time integral,

$$\int_{-\infty}^{\infty} dt e^{i(\omega_p + \omega'_p - \omega''_s - \omega'''_i)t} = 2\pi \delta(\omega_p + \omega'_p - \omega''_s - \omega'''_i). \tag{2-71}$$

The pump is in a coherent state, so the annihilation operators produce amplitudes,

$$\widehat{a}_p \widehat{a}_p |\text{pump}\rangle = \alpha_p(\omega_p) \alpha_p(\omega''_s + \omega'''_i - \omega_p), \tag{2-72}$$

and the integration over the length of the fiber results in a phase matching condition,

$$\int_0^L dz e^{-i(\Delta k(\omega, \omega'', \omega'''))z} = \text{sinc} \left[\frac{L}{2} \Delta k \right] e^{i \frac{L}{2} \Delta k(\omega, \omega'', \omega''')}, \tag{2-73}$$

Where,

$$\Delta k(\omega, \omega'', \omega''') = k_p(\omega) + k_p(\omega''_s + \omega'''_i - \omega_p) - k_s(\omega''_s) - k_i(\omega'''_i). \tag{2-74}$$

Limiting the pump photons to have the same central frequency, we find the joint spectral amplitude of the 2 photon state to be,

$$\begin{aligned}
f(\omega_s, \omega_i) &= \int d\omega \alpha_p(\omega_p) \alpha_p(\omega''_s + \omega'''_i - \omega_p) \\
&\times \text{sinc} \left[\frac{L}{2} \Delta k(\omega, \omega'', \omega''') \right] e^{i \frac{L}{2} \Delta k(\omega, \omega'', \omega''')}.
\end{aligned} \tag{2-75}$$

Depending on the particular parameters of the system, the joint spectral amplitude may or may not be factorable. If factorable, $f(\omega_i, \omega_j)$ may be separated into individual probability amplitudes for each photon,

$$f(\omega_i, \omega_j) = g_i(\omega_i)g_j(\omega_j). \quad (2-76)$$

So after heralding, the remaining photon still exists in a pure state useful for quantum information applications [7, 8]. If $f(\omega_i, \omega_j)$ is not factorable, the photons cannot be described individually, and their entangled nature may be used in many applications [33].

CHAPTER III

HOLLOW-CORE OPTICAL FIBERS

The previous section provided the mathematical framework for how entangled photons can be generated by degenerate four-wave mixing (FWM), highlighting that the efficient generation of the fields requires a high nonlinearity of the material, long interaction lengths, and high peak pump powers. A waveguide can help achieve the long interaction lengths and high peak pump powers while providing the necessary phase matching for degenerate FWM. To create a system capable of tunable control over the frequencies of the generated correlated photons, the unique properties of a particular type of waveguide, the hollow-core photonic bandgap fiber, will be exploited. This chapter will serve as an overview of the waveguide, highlighting how the hollow-core allows a filling fluid to provide the nonlinearity and how the photonic crystal surrounding the core can be used to tune the properties of the fiber.

The underlying concept for hollow core photonic bandgap (HC-PBG) fibers can be traced to the 1970s in a series of papers by Yeh and Yariv [34-36], where the idea of using a pattern of materials of different refractive indices to form a waveguide was developed. A physical realization of these fibers was performed by Cregan a few decades later [16]. After those initial papers, the field developed, with the theory of guidance being refined [37, 38], fabrication techniques improved, and whole new methods for guiding and trapping light being developed [37, 39].

The mechanism used by these fibers, in particular HC-PBG fibers, is vital for understanding how these fibers may be used to produce frequency tunable entangled

photons by four-wave mixing (FWM). This chapter serves as an overview of this mechanism, highlighting the aspects most relevant to the goal of the dissertation.

3.1 Brief Overview of TIR

The guidance method of HC-PBG fibers differs dramatically from standard, solid core fibers. Briefly, traditional fibers guide by total internal reflection (TIR) (see Figure 3.1), which occurs when light in a high refractive index material (like glass) encounters an interface with a low refractive index material (like air) at some incidence angle θ .

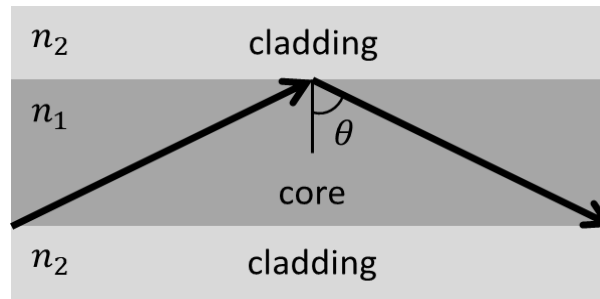


Figure 3.1. TIR in Solid Fiber: A cartoon of the guidance mechanism of a standard, solid core fiber. Light in the higher refractive index core is reflected by total internal reflection.

If the angle between the normal of the interface and the propagation direction of the light is large enough, Snell's Law tells us the light will be reflected back into the high refractive index material:

$$n_{core} \sin(\theta_{core}) = n_{cladding} \sin(\theta_{cladding}). \quad (3-1)$$

Solving for the ratio of core to cladding refractive index,

$$\frac{n_{core}}{n_{cladding}} = \frac{\sin(\theta_{cladding})}{\sin(\theta_{core})}, \quad (3-2)$$

and looking at the limiting case where $\theta_{cladding} = 0$, it can be seen that TIR only holds when,

$$\frac{n_{core}}{n_{cladding}} \geq 1. \quad (3-3)$$

Hollow-core fibers, by definition, have a low refractive index core. As such, TIR is not a viable mechanism for confining and guiding light. Instead, these fibers must rely on other methods of confining light to the fiber's core. While several mechanisms exist [40], HC-PBG fibers rely on a photonic bandgap created by a photonic crystal surrounding the hollow core.

3.2 Photonic Crystal and Bragg Scattering

A photonic crystal consists of a periodic array of refractive indices, which influence the light traveling through the crystal [41]. Mathematically describing such a system involves solving the wave equation for a periodic system with variable refractive indices over a range of frequencies and wave vectors [41]. Numerical methods have been developed for this [37, 38, 42], but an intuitive understanding of the guidance mechanism can be developed by thinking about Bragg scattering [36].

Bragg scattering is the occurrence of light scattering off of the crystalline structure of a material such that the waves interfere constructively in some common direction [43]. Consider a steady state plane wave that is normally incident to an array of atoms in 1 dimension as shown in Figure 3.2. At every atom, some amount of the light is reflected such that the total reflected wave may be written as

$$E'_{total} = rE_0e^{-i(kz+kd)} + rE_0e^{-i(kz+2kd)} + rE_0e^{-i(kz+3kd)} + \dots \quad (3-4)$$

$$= r E_0 e^{-ikz} (e^{-2ikd} + e^{-2ikd} + e^{-2ikd} + \dots)$$

where r is the reflection coefficient from the interaction with the atom.

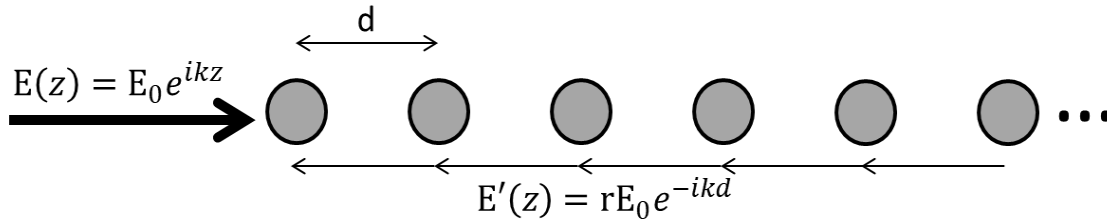


Figure 3.2. 1D Bragg Scattering: A representation of 1-dimensional Bragg scattering off elements spaced length d apart. When the reflected waves add together constructively, the incident light is effectively reflected.

If the wave vector of the light is such that the Bragg condition ($k = \frac{m\pi}{2d}$) is met, for a semi-infinite material, no matter how small r is, the light will always be reflected. A 1-dimensional photonic crystal operates in a similar way, where instead of atoms in a lattice, one period of the photonic crystal reflects some portion of the incoming light, as shown in Figure 3.3 (with the similarity to Figure 3.2 highlighted by the imaginary atoms shown).

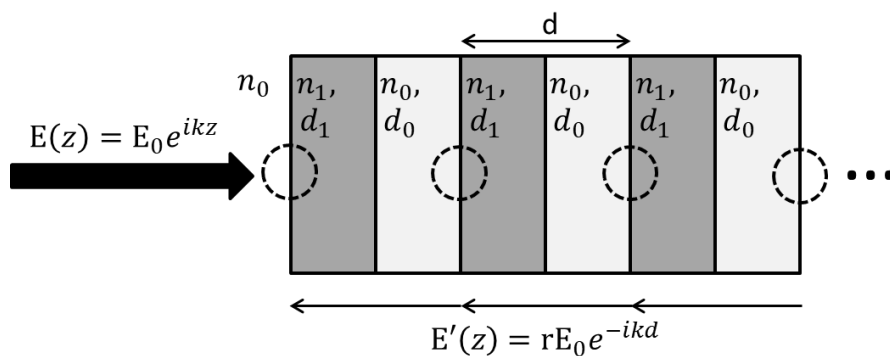


Figure 3.3. 1D Photonic Crystal: A cartoon of a 1-dimensional photonic crystal with the atomic Bragg grating of Figure 3.2 overlaid. If the total reflected waves from each optical unit add constructively, light incident will be effectively reflected.

Just as in the case with the atoms, if the reflection from each unit of the photonic crystal is such that the reflected waves add constructively, a semi-infinite photonic crystal will exhibit perfect reflection.

Qualitatively, the photonic crystal surrounding the core of a HC-BBG fiber may be thought of as a Bragg mirror encircling the core and serving to reflect light with wave vectors that are close to the Bragg condition. But quantitatively, this view runs into some difficulties. In a more realistic case of a 2-dimensional photonic crystal with a more complex geometry and light not completely perpendicular to the crystal surface, additional considerations like the polarization of the light and the range of angles of incidence must be considered [44]. Finally, to go from a photonic crystal with an outside wave incident on its surface to a waveguide transmitting light through a core, a defect will need to be added to the photonic crystal that allows for such an occurrence [35, 41].

Bloch-wave solutions found iteratively for the photonic crystals periodic structure can achieve this, and have shown an optimal design requires larger volumes of the low refractive index material to expand the range of wavelengths that can be confined in the core and a triangular lattice light design for the high refractive index material to best reflect both TE and TM polarized light [41, 42, 45]. The result is a HC-PBG fiber with a photonic crystal as shown in Figure 3.4.

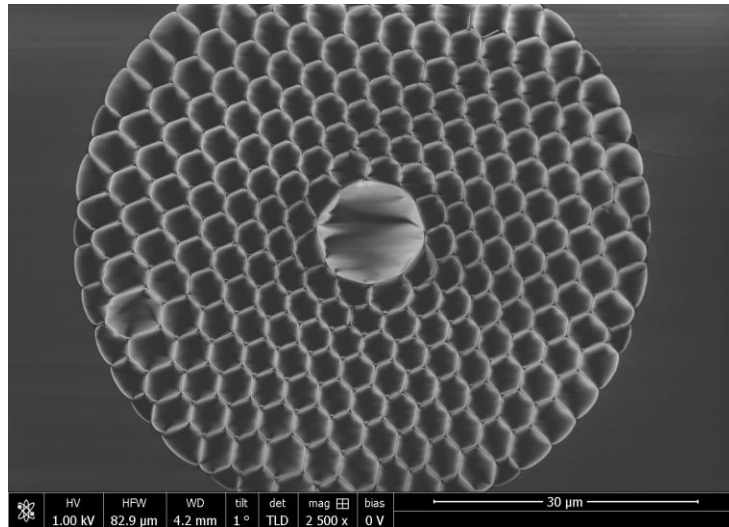


Figure 3.4. HC-PBG Fiber Face: A SEM image of the face of a HC-PBG fiber produced by Dr. Fetah Benabid and imaged at the University of Oregon, showing the $10\mu\text{m}$ core surrounded by a 2-dimensional photonic crystal comprised of large low refractive index hollow holes and narrow high refractive index connected fused silica struts.

While this work is vital for the construction of HC-PBG fibers, the conceptual model above is probably sufficient when treating the fibers as pre-manufactured waveguides.

3.3 Altering the Guidance Window by Changing Refractive Index

Because the photonic bandgap depends on the geometry of the crystal and the refractive index values of the crystal's materials, modifying any of those properties will affect the bandgap and what wavelengths of light can be effectively guided by the fiber.

It is relatively simple to change the refractive index of the low refractive index element of these fibers by replacing the air with some fluid [26], which has led to numerous experiments exploiting hollow core fibers and waveguides to study nonlinear optical interactions with fluids [19, 39, 46-49].

A scalar model was developed to predict the new guidance window of the fiber after changing the refractive index of the photonic crystal [44]:

$$\bar{\lambda} = \lambda \sqrt{\frac{n_s^2 - n_{\text{fluid}}^2}{n_s^2 - n_0^2}}. \quad (3-5)$$

Here λ represents the wavelengths of light in the guidance window, n_s is the refractive index of the silica in the photonic crystal, n_0 is the initial refractive index of the air holes of the photonic crystal, n_{fluid} is the refractive index of the filling fluid, and $\bar{\lambda}$ represents the wavelengths of light in the new guidance window. While strictly only true for scalar fields, its accuracy has been shown for fibers filled with heavy water [27].

From Equation 3-5, it can be seen that as the refractive index of the fluid increases, the wavelengths in the guidance window of the fiber will decrease. Furthermore, this shift can be seen as a mapping of the old wavelengths to the new ones. For example, if λ_0 represented the center of the guidance window, the application of Equation 3-5 would give the central wavelength of the shifted guidance window, $\bar{\lambda}_0$.

The ability to change the wavelengths guided by the HC-PBG fiber makes it an interesting candidate for a system meant to have tunability over the frequencies of light generated by FWM. By changing the refractive index of the fluid filling the fiber, new wavelengths of light are potentially made available to the nonlinear process.

3.4 Dispersion of Light in the Guidance Window

In addition to being able to be filled with fluids and have a tunable guidance window, the last feature of HC-PBG fiber that makes it so appealing for this type of work is the dispersion profile of light in the window. To achieve efficient four-wave mixing

(FWM) as described in Chapter 2, the electric fields of the light must obey both energy and phase conservation. Recall that the wave vector k is defined as,

$$k_j = \frac{n_j(\omega_j)\omega_j}{c}, \quad (3-6)$$

where the subscript, j , distinguishes the wave vector of the different fields involved in the degenerate FWM process. The phase matching condition requires the wave vectors obey

$$k_1 + k_2 - 2k_3 + 2\gamma P_3 \approx 0, \quad (3-7)$$

along with energy conservation:

$$2\omega_3 - \omega_1 - \omega_2 = 0. \quad (3-8)$$

Combining the above, and assuming perfect phase matching:

$$2 \frac{n_3(\omega_3)\omega_3}{c} - \frac{n_1(\omega_1)\omega_1}{c} - \frac{n_2(\omega_2)\omega_2}{c} = 2\gamma P_3. \quad (3-9)$$

Assuming for a moment the pump power is very weak, such that $2\gamma P_3 \approx 0$, this simplifies to,

$$2n_3(\omega_3)\omega_3 - n_1(\omega_1)\omega_1 - n_2(\omega_2)\omega_2 = 0. \quad (3-10)$$

The simplest way to achieve both phase and energy matching would be to have

$$n_1(\omega_1) = n_2(\omega_2) = n_3(\omega_3). \quad (3-11)$$

However, this isn't normally found in nature. Instead, bulk materials exhibit normal dispersion, where the phase velocity of lower frequency (longer wavelength) light travels faster through the material than higher frequency (shorter wavelength) light.

The addition of a waveguide can address this issue by modifying the dispersion of light. Within the HC-PBG fiber's guidance window, the shorter wavelengths experience normal dispersion. However, at longer wavelengths the dispersion becomes anomalous

[50]. In this domain, longer wavelengths (smaller frequency) light travels slower than shorter wavelengths.

Intuitively, this agrees with what would be expected by looking at the Kramers-Kronig relations for a structure light a HC-PBG fiber [51], where light outside of the guidance window can be thought of as being absorbed by the fiber. In such a system, the transition from absorbing to guiding at the short wavelength edge of the fiber would result in normal dispersion while the transition to absorbing at the long wavelength edge would correspond to anomalous dispersion.

The total dispersion for a fluid filled HC-PBG fiber can then be thought of as having 2 contributions, the material and waveguide elements [12]:

$$\tilde{n}_j = n_j + \Delta n_j. \quad (3-12)$$

The phase matching condition may be rewritten as,

$$\Delta k_M + \Delta k_{WG} = 2\gamma P_3, \quad (3-13)$$

where,

$$\Delta k_M = 2 \frac{n_3(\omega_3)\omega_3}{c} - \frac{n_1(\omega_1)\omega_1}{c} - \frac{n_2(\omega_2)\omega_2}{c}, \quad (3-14)$$

and

$$\Delta k_{WG} = 2 \frac{\Delta n_3(\omega_3)\omega_3}{c} - \frac{\Delta n_1(\omega_1)\omega_1}{c} - \frac{\Delta n_2(\omega_2)\omega_2}{c}. \quad (3-15)$$

When the total dispersion of the system is near 0, these terms allow phase matching to occur for select sideband frequencies, as shown in the example Figure 3.4.

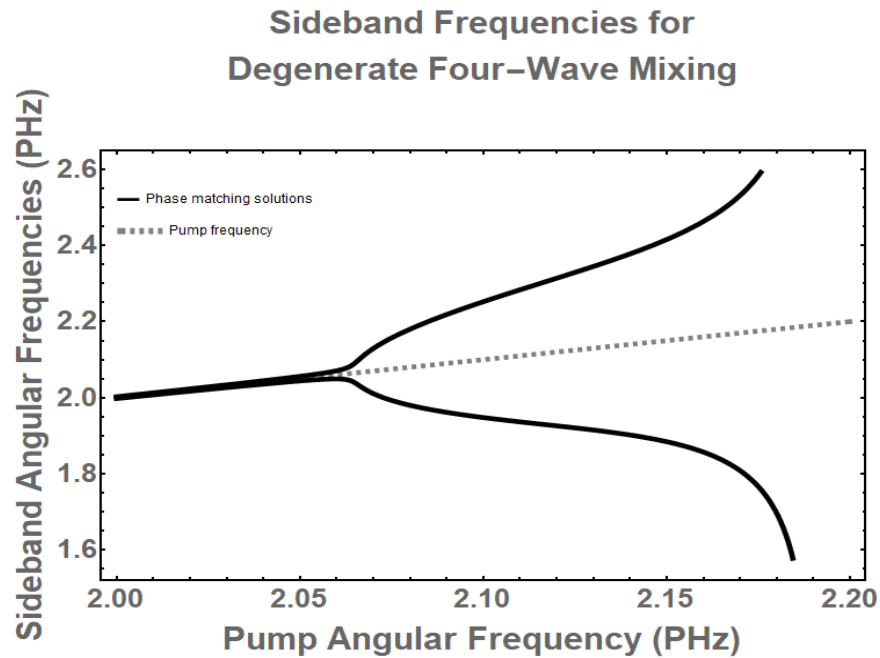


Figure 3.5. Phase Matching Solutions to Four-Wave Mixing: An example of expected frequencies of the sidebands satisfying Equations 3-8 and 3-15 for degenerate four-wave mixing when the pump is close to the zero dispersion frequency.

3.5 Birefringence

To construct these fibers, draw towers are used. Large preforms of the fiber, measuring several centimeters across, are mounted at the top of the tower and heated. Gravity pulls the glass to the bottom of the tower, where the fiber is spooled [37]. During the process, small asymmetries often develop in the core, leading it to become more elliptical than designed. This ellipticity results in the fibers becoming birefringent: polarized light along one axis of the fiber will travel at a different speed than light polarized along a different axis. If the fiber is polarization maintaining, this opens the possibility of additional phase matching opportunities by cross phase matching four-wave mixing [52].

3.6 Surface Modes

A final note on the use of photonic crystals to confine light to the hollow core of a fiber: while modes in the hollow-core at the center of the photonic fiber are excited to propagate light through the fiber, surface modes may be excited as well. These modes rest at the interface between the photonic crystal and the core and can be distinguished from core modes by having the majority of the energy stored within the high refractive index walls of the core [53].

Surface modes tend to be fairly lossy, as energy is coupled to leaky modes in the photonic crystal and out of the fiber [53]. For certain frequencies of light in the guidance window of the fiber, there can be effective coupling of energy from the core mode to these surface modes. This leads to regions of the guidance window created by the photonic crystal which are unsuitable for long range transfer of light, as the energy couples to the surface mode and from the surface mode out of the fiber.

The existence of these surface modes depends on the termination of the photonic crystal around the core of the fiber [41]. By altering or removing the walls of the core, these surface modes may be reduced or eliminated [53, 54], which has proven critical for this work, as calculations done by our collaborator Prof. Fetai Benabid's group indicated coupling between core and surface modes would dominate the guidance window with high density filling fluid.

CHAPTER IV

XENON

It was shown in the previous chapter that changing the refractive index of the air holes in the photonic crystal of a hollow-core photonic bandgap (HC-PBG) fiber changes the wavelengths of light guided by the fiber and the dispersion properties of the fiber. A fluid with a large range of refractive index values could then be used to create a tunable system for optimizing the guidance properties of the HC-PBG to produce entangled photon pairs at desired frequencies.

Additionally, the fluid needs to have a strong enough nonlinear response to have meaningful numbers of photon pairs generated by degenerate four-wave mixing (FWM). As shown in Chapter 2, the classical gain for FWM is defined as

$$G = \left| \frac{B_1(z)}{B_2(0)} \right|^2 = |\gamma P_3 z|^2, \quad (4-1)$$

with

$$\gamma = \frac{n^{(2)}\omega}{cA_{eff}} = \frac{\chi^{(3)}\omega}{ncA_{eff}}, \quad (4-2)$$

where the nonlinear coefficient γ is dependent on the nonlinear refractive index of the core ($n^{(2)}$), the frequency of the pump (ω), the speed of light (c), and the effective transverse mode of the pulse in the material (A_{eff}). The nonlinear refractive index may be written in terms of the nonlinear susceptibility of the material by,

$$n^{(2)} = \frac{\chi^{(3)}}{n}. \quad (4-3)$$

So for light confined to the core of the fiber, interacting with a material with a relatively large $\chi^{(3)}$ is necessary for generating strong enough signals to be easily detected.

4.1 Ideal Filling Fluid

A fluid with a high nonlinearity and a variable density would then be best for creating a system with tunable control over the generation of entangled photon pairs in the sideband frequencies of degenerate FWM. Liquids have high nonlinearities, but the density of liquids is very hard to change. The density of gas may be easily altered by changing the pressure, but the nonlinear response of gases is weak compared to materials like fused silica [55].

Supercritical fluids combine the high nonlinearity of liquids with the compressibility of gases. By working with a supercritical fluid, the guidance properties of the hollow-core fiber may still be tuned by varying the density of the filling fluid while the nonlinearity of the fluid in the core is sufficiently large to allow nonlinear optical processes like four-wave mixing to take place.

Finally, the guidance window of the fiber is relatively narrow: a few hundred nanometers. In order for the system to be useful for generating entangled photons, other nonlinear sources of light should be suppressed. One of the largest, and a partial motivator for this work, is Raman scattering.

4.2 Raman Scattering

A derivation of the generation of Raman light may be found in [12], but a conceptual explanation might be useful at this stage. Light is constantly interacting with the atoms of the material it is traveling through. This interaction is observed in the reduced speed of light in material, compared to the speed of light in vacuum. Rarely, the photon can participate in a scattering event that transfers some of the energy of the photon to a vibrational mode of the material and results in a photon with less energy [28]. This is Stokes scattering and, depending on the available vibrational modes in the material, can reduce the energy in the light by discrete amounts (hydrogen gas [56]) or in a continuum (fused silica [12]). The opposite may also occur, named anti-Stokes scattering, where energy from a vibrational mode is added to the emitted light, but this is less likely at room temperature materials [28]. The amount of light scattered by this process is set by the number of photon-atom interactions. As such the intensity of light generated by this process is dependent on the average power of the light source.

Stokes scattering is particularly noticeable in fiber systems, where the high intensity pump light is interacting with the silica-glass material of the core of the fiber over long distances [12]. If the frequencies generated by Stokes or anti-Stokes scattering overlap the frequencies produced by a process light FWM, it is difficult to distinguish between the two. Any desire to see correlations between photons will be hampered, as the Raman light will appear as noise in the same frequency band as the desired signal. To avoid this issue, systems for producing entangled photons from four-wave mixing in solid core fibers normally are designed to generate the photon pairs at frequencies substantially different than the pump [12] or very close to the pump [57] to reduce the

overlap between the generated sidebands from the FWM and the Raman light produced by Stokes scattering from the pump.

The relatively small guidance window of a hollow-core photonic bandgap fiber means light generated from Raman scattering can occupy large sections of the available frequencies for generating light from FWM. An ideal material for filling these fibers would then, in addition to have a strong nonlinear response and wide range of accessible refractive index values, be incapable of generating Stokes and anti-Stokes light from Raman scattering.

The noble gases have just this sort of property. Singular atoms with full electron shells, these gases have no rotational vibrational modes and therefore no mechanism for Raman scattering [17]. And while a very small concentration of xenon atoms form diatomic molecules, the Raman spectrum from these is expected to be both minimal and have narrow spectral overlaps with the guidance window.

4.3 Noble Properties

Of the noble gases, xenon has the largest nonlinear optical response while being stable (e.g. not radon), as shown in Table 4.1 [58].

Table 4.1. Nonlinear Polarizability of Noble Gases: Measurements of the nonlinear polarizability of noble gases showing xenon the most nonlinear by almost a factor of 3 [58].

	Helium	Neon	Argon	Krypton	Xenon
$\chi^{(3)}$	3.43	6.18	80.60	219.52	644.84
	$\times 10^{-28} \frac{m^2}{V^2}$	$\times 10^{-28} \frac{m^2}{V^2}$	$\times 10^{-28} \frac{m^2}{V^2}$	$\times 10^{-28} \frac{m^2}{V^2}$	$\times 10^{-28} \frac{m^2}{V^2}$

Because of this high nonlinear response compared to the other noble gases, the concentration of xenon fluid necessary to provide a viable nonlinear material will be less than that of the other gases, making it an easier system to achieve.

Xenon is able to provide both a strong nonlinear response and a wide range of refractive index values thanks to its transition from a gas to a supercritical fluid. This transition is readily accessible with standard laboratory equipment, with a critical point of 16.6 °C and 57.6 atm. Operating at room temperature, it is possible to increase the pressure of xenon to traverse through the gaseous stage and enter the supercritical regime, as can be seen in Figure 4.1.

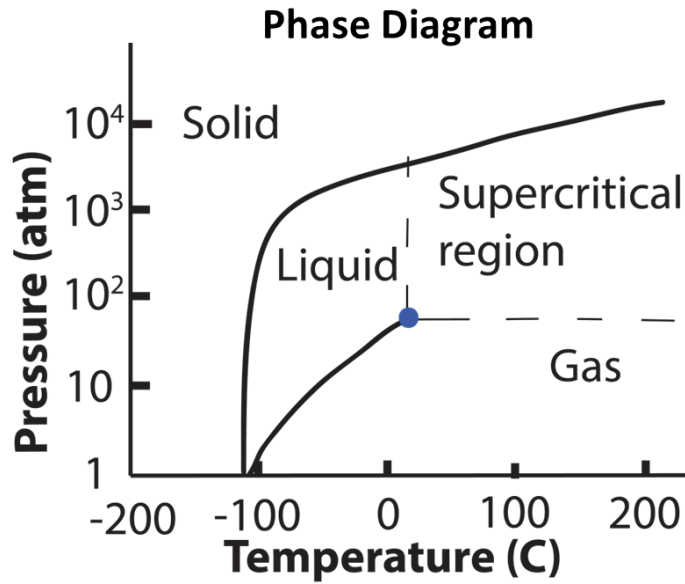


Figure 4.1. The Phase Diagram of Xenon: A cartoon of the phase diagram of xenon highlighting the critical point at 16.6 °C and 57.6 atm.

During this transition, the relationship between the density of xenon and the pressure of the xenon becomes highly nonlinear, as shown in Figure 4.2. At low pressures, gases obey the ideal gas law,

$$PM = \rho RT, \quad (4-4)$$

where P is the pressure, M is the molar mass (for xenon: 131.3 g/mol), ρ is the density, R is the ideal gas constant, and T is the temperature. But, as the xenon fluid approaches the supercritical regime, the density of xenon increases at a much greater rate with respect to pressure. Realistic values for the xenon density as a function of pressure were given by NIST measurements [59].

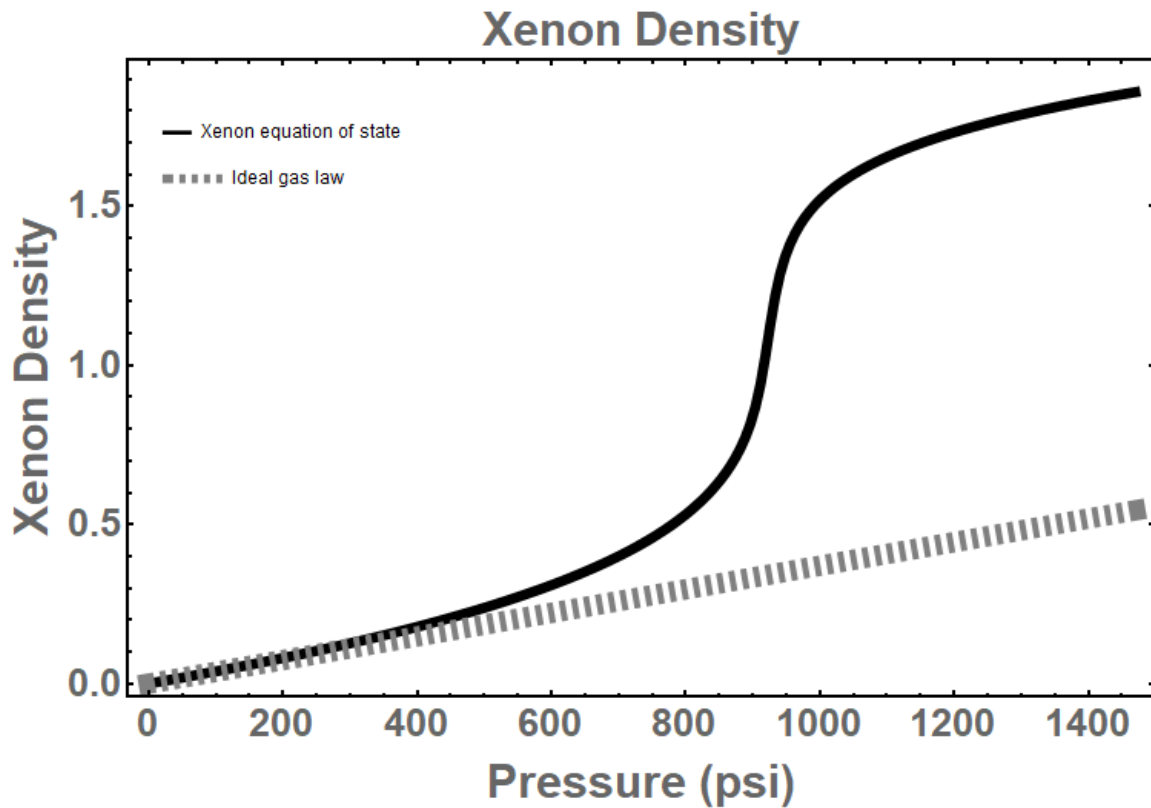


Figure 4.2. Xenon Density Equation of State: A plot of the xenon density as a function of pressure from the realistic equation of state compared to the density of an ideal gas.

Because both the linear and nonlinear refractive index of xenon depend on its density [60], this enhancement of the density of the xenon during the phase transition is the key feature that makes xenon such a good choice of filling fluid for generating tunable entangled photons in the hollow-core photonic bandgap fiber. At supercritical pressures, the nonlinear refractive index of silica approaches that of fused silica while also offering substantial control over the guidance properties of the photonic crystal [18]. Even at 950 psi, the nonlinearity is nearly 250 times greater than at standard temperature and pressure (STP), and becomes large enough to allow for the generation of observable

fields from four-wave mixing given the equipment and constraints of the lab were the work was performed.

The refractive index of xenon at a given wavelength and density of fluid may be found by solving a Lorentz-Lorenz equation developed by modifying the dilute-gas Sellmeier equation [60],

$$\frac{n_{XE}(\lambda)^2 - 1}{n_{XE}(\lambda)^2 + 2} = \left(\frac{2}{3}\right) 0.012055 \left(\frac{0.26783}{43.741 - 1/\lambda^2} + \frac{0.29481}{57.480 - 1/\lambda^2} + \frac{5.0333}{112.74 - 1/\lambda^2} \right) \left(\frac{\rho_{XE}}{\rho_0} \right), \quad (4-5)$$

where ρ_{XE} is the density of xenon, ρ_0 is the density of xenon at STP, $n_{XE}(\lambda)$ is the wavelength dependent refractive index at that density, and λ is the wavelength in microns. For reference, the refractive index of xenon as a function of wavelength at STP is plotted in Figure 4.3

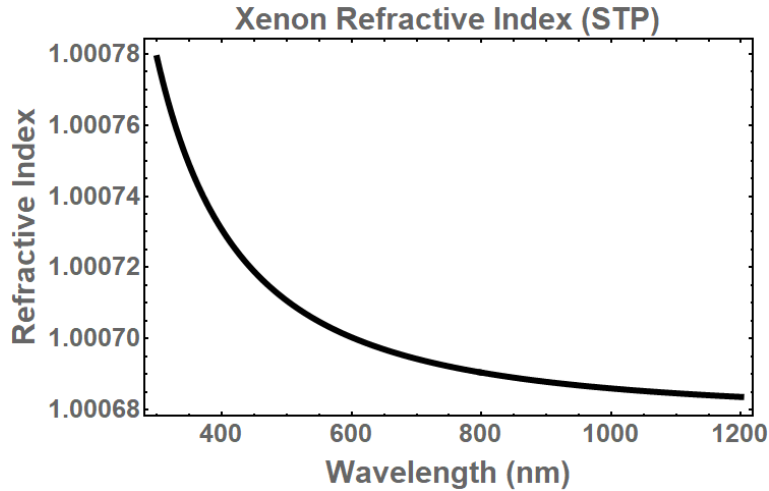


Figure 4.3. Xenon Phase Refractive Index: Plot of the wavelength dependence of the phase refractive index of xenon at standard temperatures and pressures (STP) from Equation 4-5. The reduction in refractive index with increased wavelength demonstrates normal dispersion, and the gradual flattening of the dispersion curve with longer wavelengths is typical of bulk materials.

Coupling this with the scalar theory from Chapter 3, it can be shown (see Chapter 6) that the guidance window of a HC-PBG fiber can be substantially shifted in wavelength by varying the xenon pressure within the fiber. Shifting this window is the first step towards creating a system that can produce tuned entangled photons.

CHAPTER V

PROTOTYPE DESIGN

Xenon is extremely rare in the atmosphere, representing just .0000087% of its chemical composition [61]. Relatedly, xenon is expensive and sold in commercial tanks at pressures ranging from (around 40-60 atm) below those needed for this work (80-90 atm). To be able to reach desired pressures of xenon and to recycle and reuse xenon for multiple experiments, some effort was made to create a closed system for the hollow-core photonic bandgap (HC-PBG) fiber. To accomplish this, an apparatus was built to hold the supercritical xenon and control the pressure of xenon in various sections of the system by using liquid nitrogen (LN₂). This containment system was connected to cells designed to surround the HC-PBG fiber and bathe it in xenon, allowing the fluid to flow into the hollow sections of the fiber from either end. This chapter discusses the design of these elements.

5.1 Xenon Containment System

In order to be able to effectively store and reuse xenon for filling various fibers, a closed system was designed that made use of xenon's melting point being warmer than the temperature of liquid nitrogen [62]. The system needed to be able to evacuate air from sections exposed the atmosphere when a fiber was installed into the system and also effectively control the density of xenon at the fiber by regulating the pressure in the cell holding the fiber.

To accomplish these goals, a system with 3 main compartments and numerous valves was built, as shown in Figure 5.1.

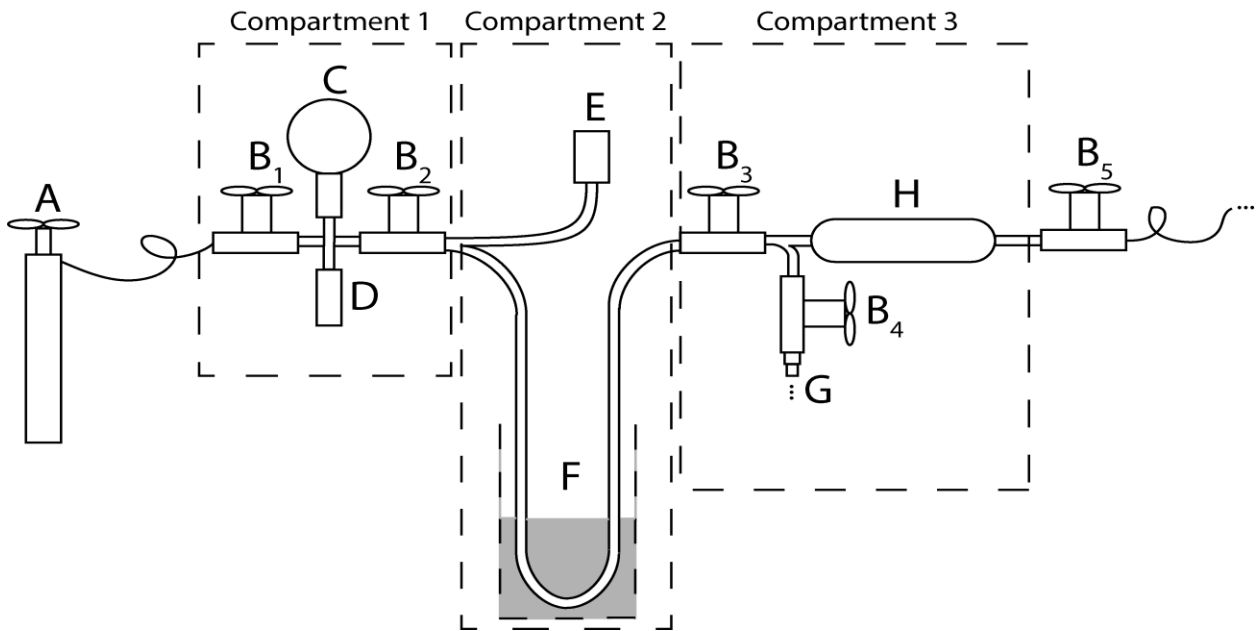


Figure 5.1. Xenon Containment System: Diagram of the xenon containment system used to extract xenon from a low-pressure commercial tank, store xenon between experiments and during fiber evacuations, and transfer xenon to the cell containing the hollow core fiber

Initially, the system was evacuated via a vacuum pump connected at (G). Then, xenon gas from a commercially purchased tank (A) could be drawn into the system. Compartment 1 consisted of a small volume (D) and a series of valves (B₁ and B₂) allowed for discrete amounts of gas to be introduced into the system while a pressure gauge (C) could be used to monitor the pressure of gas in either the commercial tank (A) or the rest of the system.

Once the pressure of xenon in the apparatus was equal or greater than the pressure of xenon gas left in the commercial tank, the pressure in compartment 2 could be reduced by placing the U-tube (F) in LN₂. This froze the xenon, lowering the pressure and

allowing the filling to resume. An emergency relief valve (E) insured the xenon never accidentally reached a dangerous pressure. Once the desired amount of xenon had been drawn into compartment 2, valve B₁ could be sealed, the LN₂ bath removed, and the xenon allowed to warm to room temperature. The third compartment contained chamber (H), which allowed for discrete units of xenon to be transferred to the fiber cell through valve (B₅) in a similar manner to how volume (D) was used in compartment 1.

Should the fiber need to be replaced, the xenon could be drawn back into compartment 2 via the LN₂ trap (F), the valve (B₃) sealed. The remaining portion of the system could then safely break vacuum while the fiber was being replaced. Once completed, the vacuum pump at (G) was used to evacuate the rest of the system.

If the xenon in the apparatus was not at a sufficient pressure, a hot water bath could be placed around U-tube (F) to increase xenon pressure in compartment 2. Through regulation of valves B₃ and B₅, the pressure in the fiber could then be increased.

5.2 Fiber Cells

With a system for reaching and regulating supercritical xenon pressures constructed, the other main component needed for this work was a way to fill the HC-PBG fiber with xenon while still allowing for optical coupling of light into and out of the fiber's core. In order to subject the fiber to the smallest amount of stress, the final design consisted of a cell that placed the fiber in a bath of xenon. This kept the pressure inside the fiber equal to the pressure outside the fiber.

Depending on the length of fiber being used, two different cells were constructed. Both made use of commercially available pipe fittings and tubing to keep costs down and

to allow for modifications and adaptations. Of central importance was keeping the HC-PBG fiber stationary and available for optical coupling while the cell was being filled with xenon.

For short lengths of fiber, a cell made completely out of pipe and tube fittings was constructed. A representation of this cell is shown in Figure 5.2.

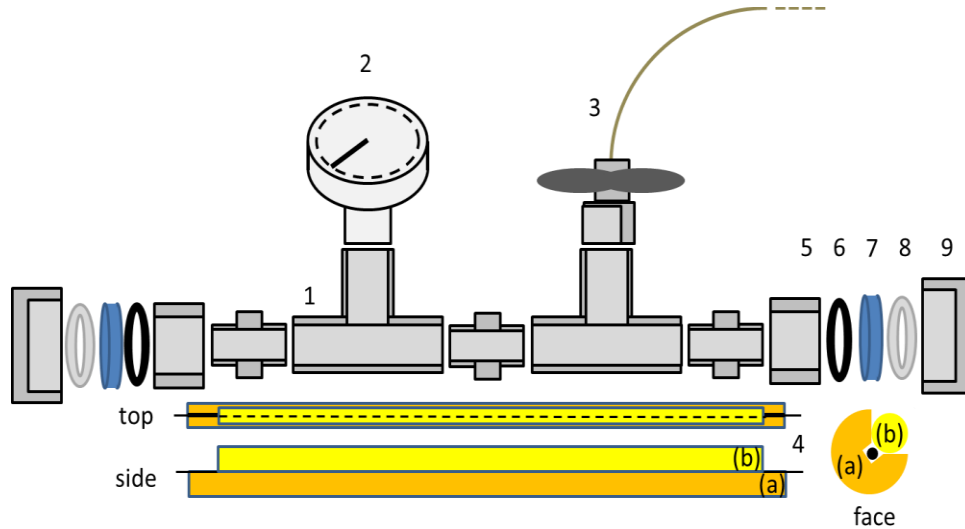


Figure 5. 2. Short Fiber Cell: Diagram of the fiber cell used for 15cm pieces of fiber, securing the fiber in a bath of xenon while allowing optical coupling of light through the fiber.

The main body was 16 cm long and made of 3/8" pipe fittings and adapters (1). A pressure gauge (2) was installed to allow monitoring of the fiber pressure when the cell was sealed off from the rest of the xenon filling apparatus. The cell was connected to the rest of the xenon filling apparatus by PEEK™ tubing and could be sealed from the rest of the filling system by a valve (3) after a desired pressure of xenon was achieved.

Because xenon was being introduced and removed through valve (3), changes in the pressure of xenon resulted in forces on the fiber within the cell. An unsecured fiber could be easily moved out of laser coupling range by the flowing xenon. To address this

issue, a mount needed to be developed that could secure the fiber during changes in xenon pressure.

To do this, a removable platform was machined to hold the fiber in the cell (4). It consisted of two parts: (a) a longer 3/4th brass cylinder lower section with a groove for the fiber to rest in and (b) a shorter nickel rod machined to be placed over the fiber in the groove, gently pressing on the fiber and securing it in place via friction. The platform was machined to just fit inside the cell, using the friction between the platform and the inner diameter of the cell to secure the rod onto the cylinder platform.

To allow for optical coupling in and out of the fiber, optical windows needed to be installed at either end of the cell. To form an airtight seal, a VCO adapter (4) was used. A rubber O-ring (5) fit the groove of the VCO adapter and pressed against a 6mm fused silica window (7). A machined Teflon washer (8) was placed between the window and the VCO nut (9) to help protect the window from damage while tightening the nut onto the cell.

For longer sections of fiber, it became necessary to modify the cell to allow the fiber to be coiled. The above cell was adapted by including PEEK™ tubing. The addition of the PEEK™ also changed the way the fiber was secured in the cell, requiring the addition of a second clamp at the head of the fiber as shown in Figure 5.3.

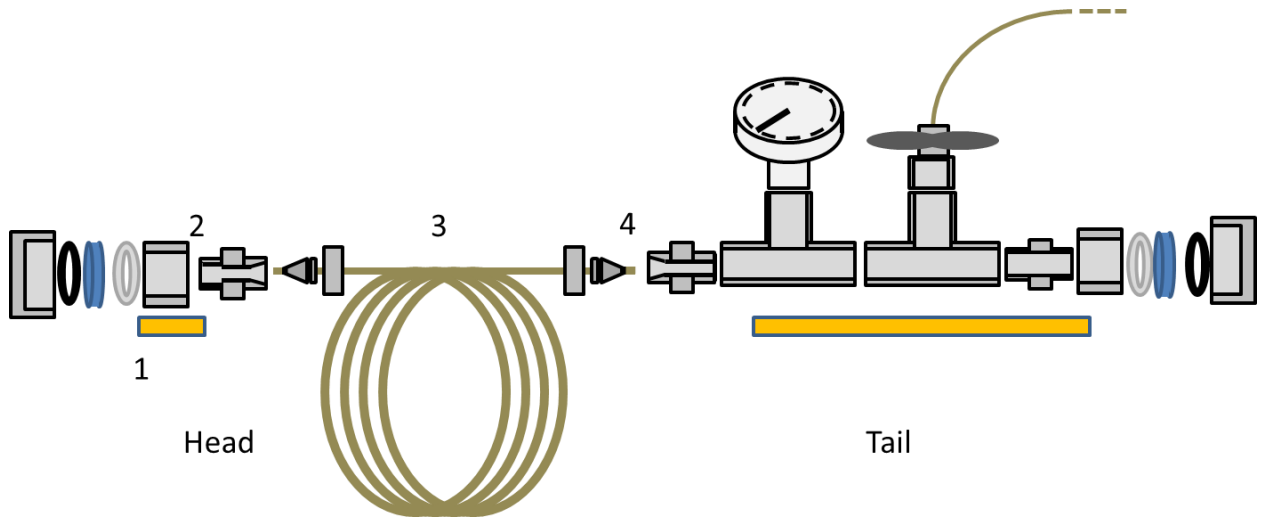


Figure 5.3. Long Fiber Cell: Diagram of the cell variant for long sections of fiber. The inclusion of tubing necessitated a second smaller cell with its own fiber mount for the head of the fiber, as well as an additional procedure for inserting the fiber into the cell.

A standard fiber chuck from Thorlabs (1) was machined to fit a small head-cell constructed from pipe fittings with VCO and Swagelok ends (2). PEEK™ tubing (3) of the desired length connected this head-cell to the tail-cell: the short length fiber cell now modified with a Swagelok adapter (4).

To install the fiber into the long fiber cell, the front of the fiber was first placed into the fiber chuck and inserted into the head-cell before the PEEK™ tubing was attached. Care was taken with installing the fiber into the PEEK™, as attempting to push the fiber through the PEEK™ ran the risk of breaking the fiber if friction between the fiber and the tubing stopped the progress of the fiber and caused a kink.

To avoid this issue, a prep line of copper wire was first fed through the PEEK™. Once this had been successfully passed through the length of tubing, the HC-PBG fiber was attached to the copper wire at one end, and the wire pulled through the PEEK™ tubing.

This allowed the fiber to be drawn, rather than pushed, through the PEEK™ tubing and avoided the possibility of friction related kinks and damages. Finally, the end of the fiber was placed on the original platform and installed in the tail-cell.

5.3 Filling the Fiber

Care was taken when pressurizing or depressurizing the fiber in the cell to minimize the pressure differentials in the fiber. Because the core of the fiber has a diameter roughly 10x that of the photonic crystal holes, the pressure in the core will reach equilibrium with the pressure of the cell in less time than the photonic crystal [63, 64]. The rate at which the holes in the fiber will reach equilibrium with the pressure of the cell can be determined from flow rate models where the mass flow rate, m , may be written as [64]:

$$m = C \times d^4 \times \Delta P^2 l, \quad (5-1)$$

with d being the diameter of the hole, ΔP being the difference in pressure between the face of the fiber and the midpoint, and C being a constant incorporating all the unchanging properties of the system, such as length of the fiber, the gas constant, etc.

It was found that the holes in the photonic crystal would take several minutes to reach equilibrium. For a system where the fiber is being filled from both ends, the point of greatest pressure difference between the core and the photonic crystal holes will be in the center of the fiber. The force of this pressure differential is relatively small, and the probability of structural failure of the core wall depends on the characteristic strength of the fused silica [65] and the shape of the core walls. To avoid needing to fully calculate this failure force, the xenon pressure differential between the cells and the photonic

crystal at the center of the fiber was kept low by regulating the pressure increase of the fiber cells. Small pressure changes of around 10 psi were allowed to take place in the cell, then the photonic crystal's pressure was allowed to equilibrate over 5 minutes before the next pressure change was performed. To fill the fiber from vacuum to 1300 psi, an ideal application of this procedure would reach the desired pressure in 10.8 hours.

CHAPTER VI

TUNING GUIDANCE WINDOW WITH SUPER-CRITICAL XENON

In order to achieve tunable entangled photons, the filling fluid in the fiber would need to have a large enough working range in refractive index that the guidance window of the fiber could be substantially altered, as discussed in Chapter 3. Xenon's transition from gas to supercritical fluid offers such a dynamic range. Using the scalar method from [27] shown in Chapter 3 as Equation 3-5, it was predicted the guidance window could be effectively transitioned over 200 nm within the operating range of the fiber cell,

$$\bar{\lambda} = \lambda \sqrt{\frac{n_s^2 - n_{\text{fluid}}^2}{n_s^2 - n_0^2}}, \quad (6-1)$$

where wavelengths of the guidance window under vacuum (λ) can be mapped to the wavelengths in the guidance window when filled with fluid ($\bar{\lambda}$) by a simple scaling function dependent on the refractive index of the silica of the photonic crystal (n_s) and refractive index of the holes of the photonic crystal under vacuum (n_0) and with the fluid (n_{fluid}).

Of particular interest was the tunability of the guidance window after the supercritical transition, when the nonlinearity of the xenon would be high enough for observing optical nonlinear effects such as four-wave mixing (FWM). However, the scalar model was expected to stop being valid as the refractive index of the filling fluid approached that of the fused silica. To both verify the scalar model still held for supercritical fluids and to measure the tunability of the guidance window at higher

pressures, recordings of the guidance window of the fiber were taken at many pressures, ranging from 0 to 1290 psi.

Work presented in this chapter summarizes and extends results previously published in [18], with a new fiber.

6.1 Experimental Setup

A FemtoPower1060 Supercontinuum Laser Source from NKT Photonics was used as a white light source (WLS) to generate a broad spectrum of 20 MHz pulsed 6 ps light ranging in wavelength from at least 500 nm to 1100 nm. The actual spectral range was much broader, but coatings on optical elements and sensitivity limits of the spectrometer limited measurements. The light from the WLS was coupled to a 15 cm HC-PBG fiber fabricated by Dr. Rodrigo Amezcua Correa with a guidance window centered around 1064 nm, constructed with modified core walls to be surface mode free [54]. The length of the fiber was not critical to the experiment, needing only to be sufficiently long to allow light not in the guidance window of the fiber to propagate through the photonic crystal and escape the fiber.

At the output of the fiber, a second lens collimated the remaining light. After additional optical elements, the output light was measured by a spectrometer to record the guidance window of the fiber, as shown in Figure 6.1.

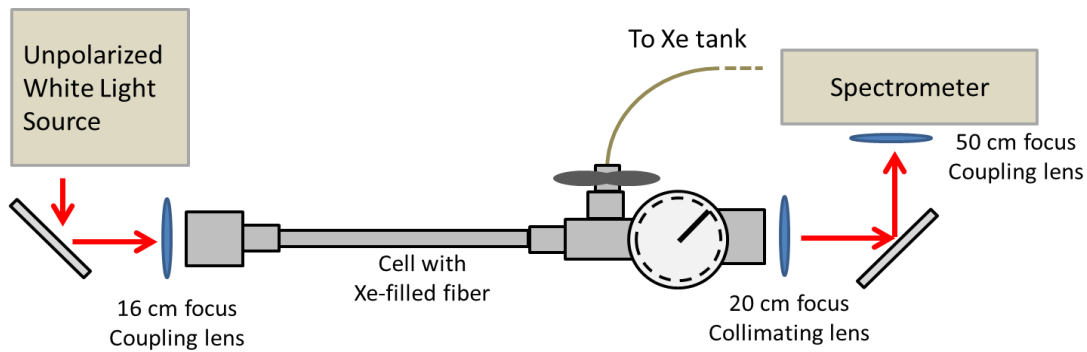


Figure 6.1. Guidance Window Experimental Setup: Cartoon of the experimental setup for measuring the guidance window of the fiber at various pressures of xenon.

The upper working range of the spectrometer used to record the spectrum of light transmitted through the xenon filled fiber was 1030 nm, meaning only a portion of the guidance window was observable at low pressures of xenon (see Figure 6.2).

Because of this, the short wavelength edge of the guidance window was chosen as an easily measurable feature of the guidance window to track as the pressure of xenon within the fiber increased and compare with the scalar theory from Equation 6-1.

6.2 Measuring Guidance Window Edge

Once the system was appropriately aligned, the HC-PBG fiber and its cell were evacuated. When sufficiently purged, xenon was slowly released into the fiber cell and allowed to fill the fiber to the desired pressure. The output spectrum of the HC-PBG fiber was recorded on the spectrometer, as shown in Figure 6.2.

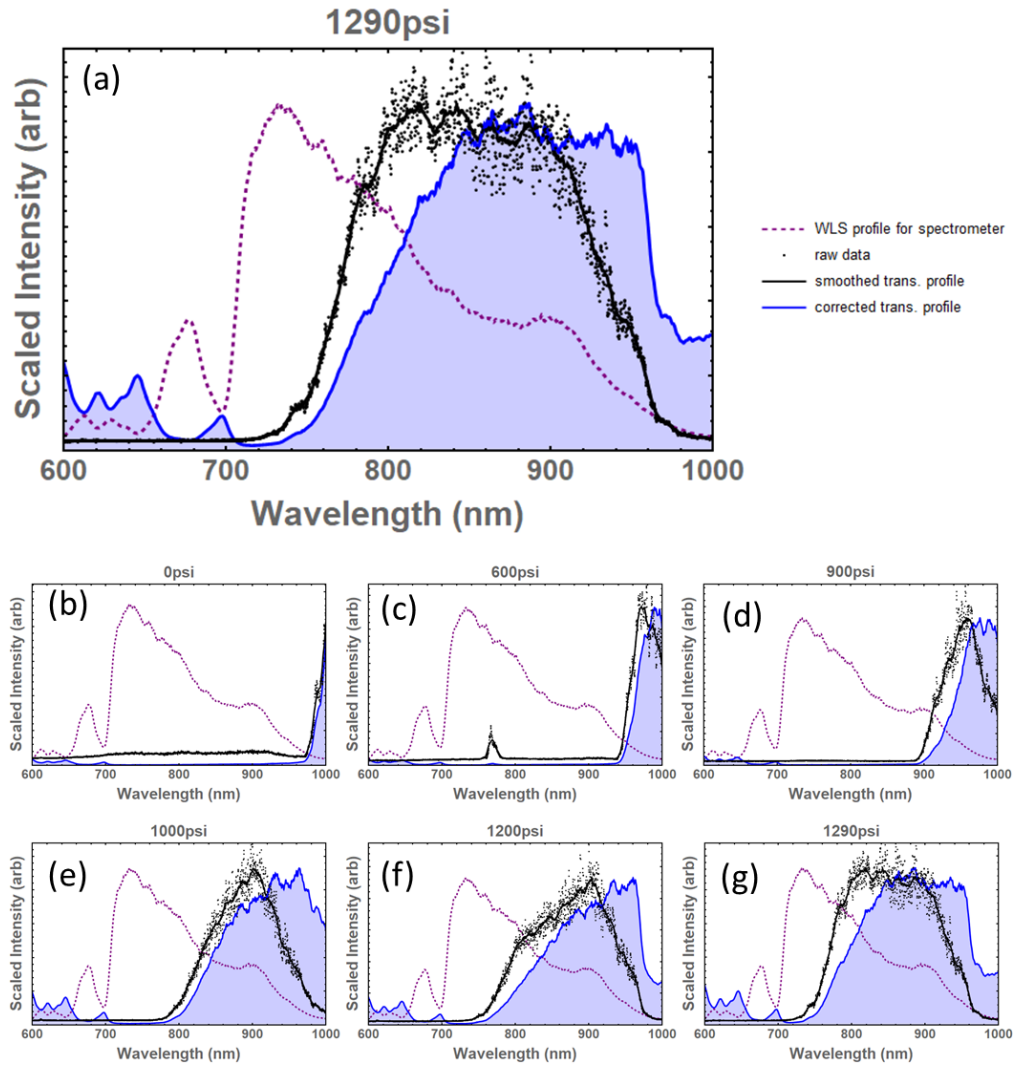


Figure 6.2. Guidance Window Spectrum vs Pressure: The measured and extracted guidance window of the HC-PBG fiber at 6 different pressures. Subfigure (a) provides a detailed view at the guidance window spectrum at a higher pressure, where the measured WLS spectrum is used to back out the fiber's guidance window from the measured spectrum. Subfigures (b)-(g) show the shift in the guidance window to shorter wavelengths as pressure of xenon increases.

The observed intensity of different wavelengths transmitted by the hollow core fiber would depend on three elements:

- 1) the efficiency of the detector at that wavelength,
- 2) the transmission efficiency of the fiber at that wavelength, and
- 3) the input intensity of light from the WLS.

To have the spectrometer measurements give an accurate representation of the guidance window of the fiber, elements (1) and (3) needed to be accounted for. To do this, the spectrum of the WLS was recorded prior to coupling into the xenon filled fiber (purple dashed line in Figure 6.2). This measurement showed the combined effects of a nonuniform input spectrum from the WLS and the nonuniform detection efficiency of the spectrometer.

Once the spectrum of light leaving the xenon fiber was recorded (black data points and smoothed curve in Figure 6.2), this pre-xenon measurement was used to back out the effects (1) and (3), leaving only (2). From this corrected spectrum (shown as the blue, shaded curve in Figure 6.2), the edge of the guidance window was defined as being at 5% the maximum intensity of the measured guidance window, although the observed trend was not particularly sensitive to how the edge of the guidance window was defined.

The effect of this correction was a guidance window edge located at a slightly longer wavelength than the raw data would suggest, as exemplified in Figure 6.2.

6.3 Comparing to Theoretical Model

The density-dependent Sellmeier equation for the xenon refractive index, Equation 4-5, was used to determine the linear refractive index of the xenon as a function of pressure and combined with the scalar model shown in Equation 6-1 to predict the xenon refractive index as a function of pressure, as also shown in our publication [18]. Defining the guidance window edge as starting at 5% the maximum intensity of the measured light from the guidance window as observed by the spectrometer, the experimental shift in the edge of the guidance window could be compared to theoretical predictions using xenon's known equation of state or an ideal gas. The results are shown in Figure 6.3.

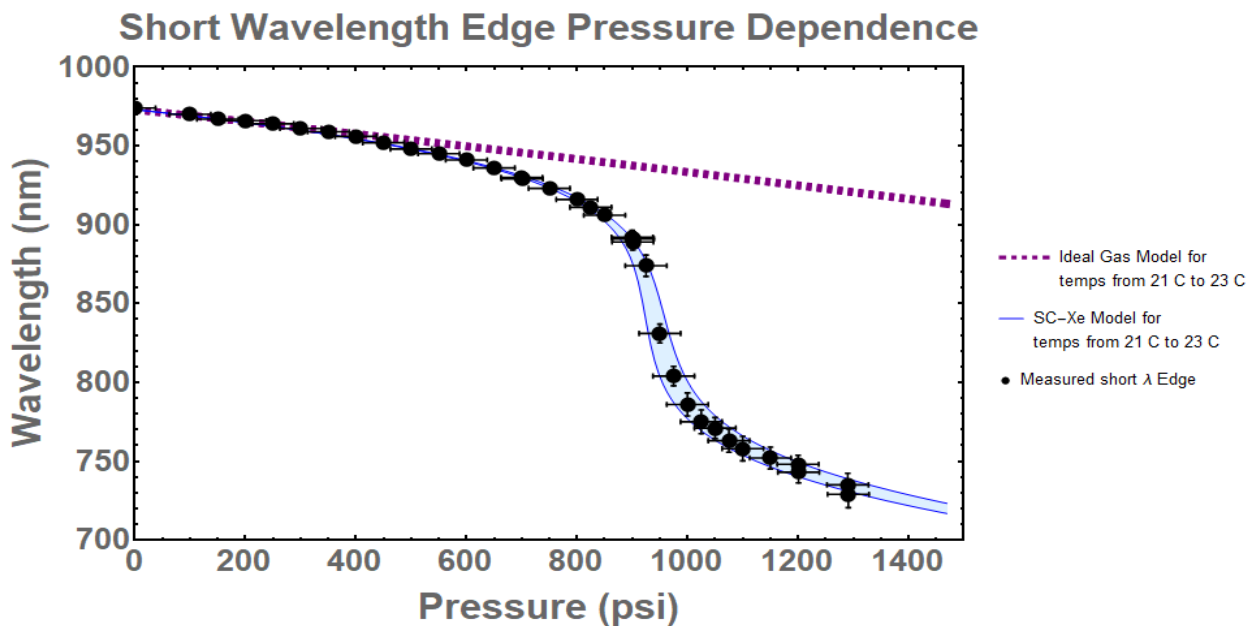


Figure 6.3. Guidance Window Edge vs Theory. Plot showing the short wavelength edge of the guidance window agreeing with a scalar theory using the xenon equation of state. The nonlinear nature of the curve corresponds to the transition of the xenon from a gas to supercritical xenon and may be compared to a model based on the ideal gas law.

Error bars on the horizontal axis due to the pressure gauge having a 5% accuracy error. Error bars on vertical axis represent at +/-2% choice in the definition of the intensity of the start of the guidance window compared to the maximum intensity of the spectrum. Temperature of xenon fit to data, and agrees with working around lab temperature. The strong agreement between the scalar model predictions and the measured edge of the guidance window validates the use of the model for supercritical xenon. The guidance window edge was tuned over 200 nm from an initial location of 975 nm at vacuum to 740 nm at 1290 psi.

The transition to supercritical fluid was stretched over a range of over 150psi because of the temperature of the system. The critical point of xenon is at 16.6 °C. By working at a lab temperature of ~22 °C, the transmission was made more gradual. By staying away from the step-like density transition that occurs near the critical point, xenon densities along this transition curve are available choices for tuning the guidance window to guide the wavelengths of the desired entangled photon pairs.

At 950 psi, the nonlinearity of the xenon in the core of the fiber was estimated to be $n_2 = \frac{1.45 \times 10^{-16} \text{cm}^2}{W}$, which is sufficient under our experimental constraints to observe nonlinear optical effects like FWM. Past this pressure, the guidance window was still tunable over 100 nm.

The upshot of that result is that the system's guidance window can be tuned over a substantial wavelength range to choose the window of wavelengths where the correlated photons would be produced.

CHAPTER VII

TUNING DISPERSION PROFILE WITH SUPER-CRITICAL XENON

In addition to controlling the guidance window of the hollow-core photonic bandgap (HC-PBG) fiber, the density of xenon within the fiber is also expected to alter the dispersion profile of the guidance window. This dispersion profile, as outlined in Chapter 3, is the combination a material dispersion term dependent on the supercritical xenon in the fiber's core and a waveguide dispersion term related to the photonic crystal of the fiber. By measuring the group velocity dispersion (GVD) of the guidance window, the zero dispersion wavelength (ZDW) may be found, near which nonlinear optical processes such as degenerate four-wave mixing (FWM) may be performed [12]. This section discusses the experimental method used to measure the relative group velocity of light in the guidance window of the fiber and derive the GVD profile.

7.1 Experimental Setup

To measure the relative group velocities of light in the guidance window of the HC-PBG fiber, a Mach-Zehnder interferometer setup as shown in Figure 7.1 was used.

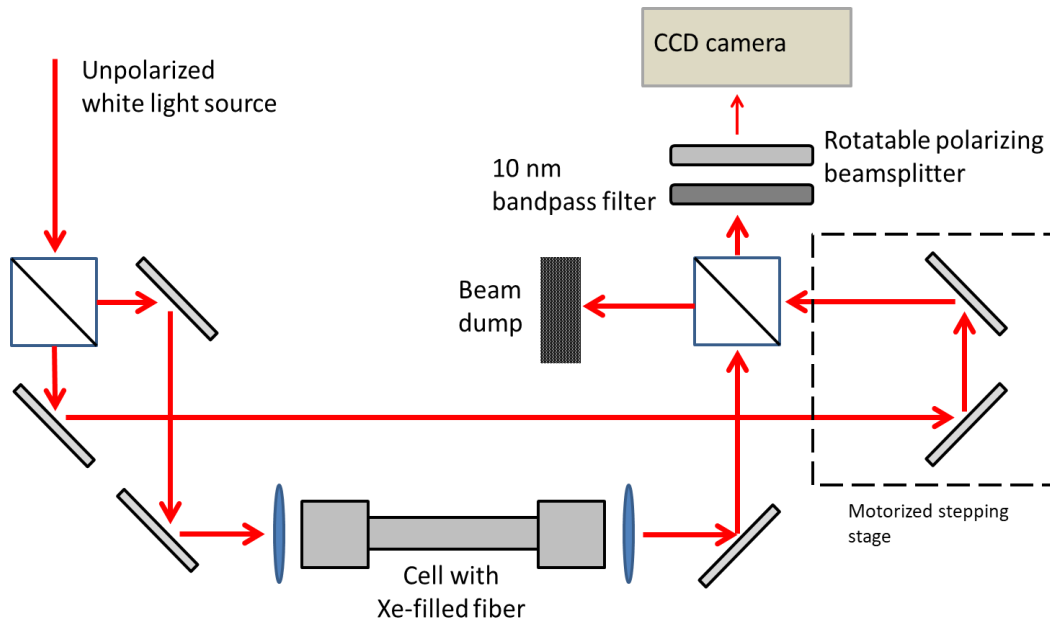


Figure 7.1. Group Velocity Setup. A diagram of the Mach-Zehnder design for measuring the relative group velocities between bands of light in the guidance window of the fiber by observing fringes from 1st-order correlations between the fields in the 2 arms.

The white light source (WLS) from the previous chapter was split along the two arms of the fiber. In one arm, the light was coupled through a 15 cm section of xenon filled HC-PBG fiber. The other arm contained a movable stage connected to a step-motor capable of minimum steps of 256 nm. Once the light was recombined on the output beamsplitter of the interferometer, various bandpass filters were used to limit the transmitted bandwidth to a 10 nm section of the light in the fiber's guidance window. The intensity profile of this transmitted light was detected on a 1-dimensional pixel array run through LabVIEW.

7.2 Measuring Group Velocity and GVD

The 10-nm bandwidth and pulsed nature of the WLS lead the light to have a short coherence length, as discussed in Chapter 2, so visible interference fringes from 1st-order correlations between the fields in the arms of the interferometer only occurred when the time delay between the arms was close to zero. When the maximum visibility of these fringes is observed, it indicates the effective optical paths of the 2 arms are equivalent.

The motorized stepping stage in the interferometer was scanned while its position and the intensity pattern on the 1-dimensional CCD camera were recorded. A slight misalignment between the 2 arms of the interferometer allowed multiple fringes to be measured on the CCD camera for every position of the motorized stage. After the measurements were complete, the visibility of the fringes at each position of the stepping stage was computed using Equation 2-29:

$$\text{visibility} = \frac{I_{\max} - I_{\min}}{I_{\max} + I_{\min}}. \quad (7-1)$$

The location of the motorized stepping stage at the maximum visibility could then be used along with knowledge of the fiber's length and group velocity properties of optical elements in the interferometer to find the relative group velocity light in that 10nm band of the fiber's guidance window. This measurement was repeated over many bands within the guidance window, and a 4th-order polynomial was fit to the group velocity measurements to model the group velocity profile (see Figure 7.2).

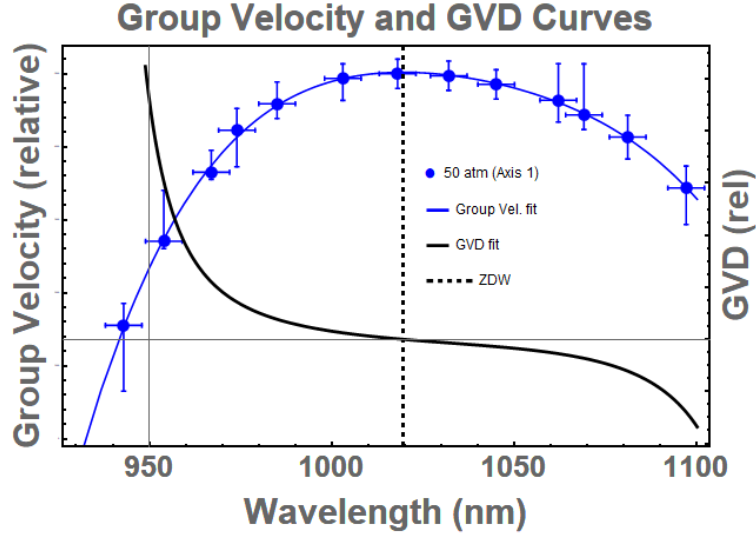


Figure 7.2. Group Velocity Measurements. A plot of the measured relative group velocity, v_g , at various wavelengths, the 4th-order polynomial fit used to describe the group velocity through the guidance window, and the GVD curve derived from the v_g polynomial curve. The ZDW is shown with a vertical dashed line to be at 1018 nm.

The horizontal error bars in the measurements of relative group velocity stem from the use of 10 nm bandpass filters. The vertical error bars are derived from the width of the visibility curve found over the stepping stage positions. The GVD curve is simple to find from the 4th-order polynomial fit of the group velocity,

$$\text{GVD} = \frac{\partial}{\partial \omega} \left(\frac{1}{v_{group}} \right). \quad (7-2)$$

From the GVD curve, the zero dispersion wavelength (ZDW) is seen when the GVD goes from having positive values (normal dispersion) to negative values (anomalous dispersion).

7.3 Birefringence

A rotatable polarizing beam splitter was used at the output of the Mach-Zehnder interferometer (see Figure 7.3) to look for any birefringence in the group velocity profile of the fiber due to asymmetries in the core dimensions. A slight birefringence was observed, highlighted by the difference in ZDW between the 2 axes.

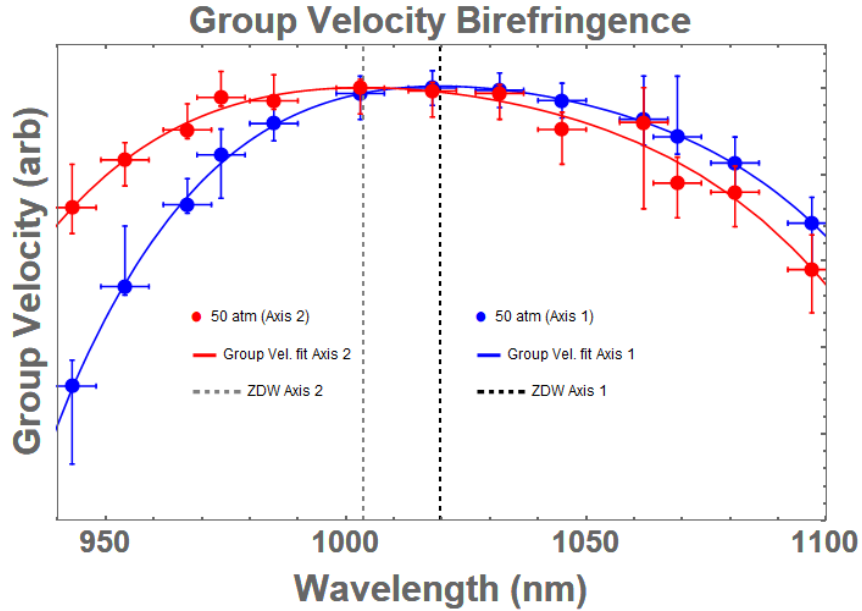


Figure 7.3. Birefringence in Group Velocity: Plots of the measured birefringence in the group velocity along the two polarization axes of the fiber. The group velocity polynomial fit and the inferred ZDW are also shown for both curves, demonstrating that the dispersion profile varies between the two axes.

The existence of birefringence opens the possibility of additional control over the frequencies of entangled photons by performing cross phase matching over both axes of the fiber [12]. However, further testing determined the fiber was not strongly polarization maintaining. This possibility is left as a potential future avenue for the work with a fiber more capable of keeping light on the two axes from mixing during propagation through

the core. For the remaining sections of this chapter, the dispersion profile along a single axis of the fiber is presented, but similar trends occurred on the other axis as well.

7.4 Dispersion Pressure Dependence

The xenon pressure was increased slowly over several pressures ranging from vacuum to 95 atm (1400 psi). Periodically, the filling of the fiber was paused to measure the relative group velocity of the guidance window of the fiber. Select group velocity measurements, polynomial fits, and ZDWs for the respective GVDs are shown in Figure 7.4.

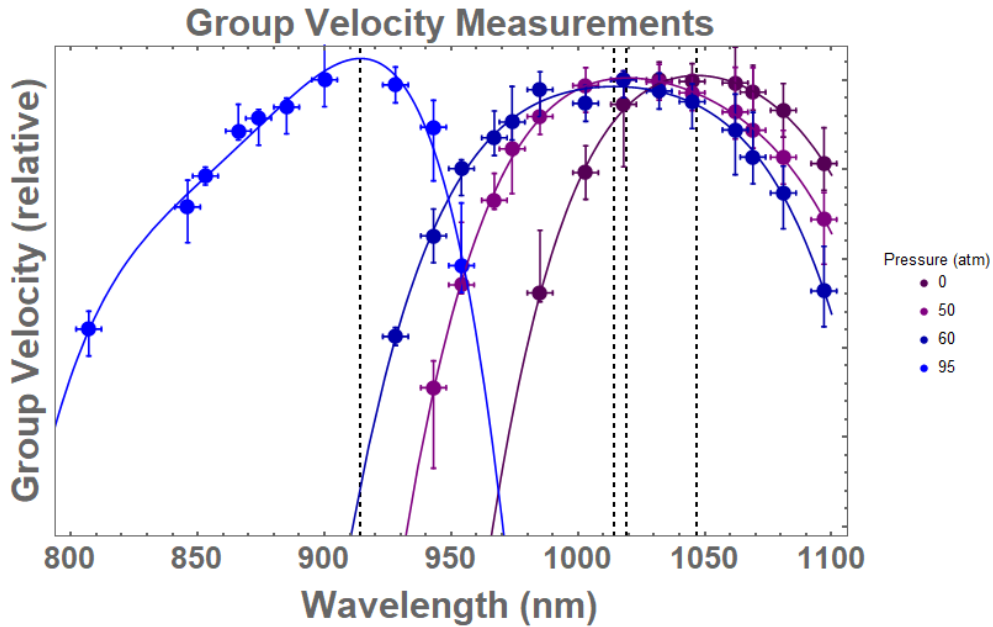


Figure 7.4. Group Velocity Curves at Various Pressures: The measured relative group velocities, polynomial fits, and inferred ZDWs for 4 pressures are plotted. The v_g polynomial curve becomes symmetrical due to the material dispersion contribution of the xenon core.

The ZDW can be seen to shift to shorter wavelengths with increased density of xenon in the HC-PBG fiber. This is opposite the shift observed in other hollow-core

fibers, such as Kagome [47]. The difference can be explained by the different guidance mechanism of HC-PBG fibers, and will be discussed in greater detail in the next chapter. Qualitatively, this wavelength shift is similar to the guidance window edge shift so well modeled by the scalar theory in the previous chapter.

However, quantitatively the ZDW shift lags behind the guidance window edge shift. In addition, the profile of the group velocity develops a pronounced asymmetry at high pressures of xenon. Both these developments may be attributed to the material dispersion of the xenon in the core of the fiber. A model encompassing this dispersion is described in the following chapter and is capable of predicting the dispersion profile of the fiber as a function of pressure in a way similar to the scalar model.

Finally, while the GVD's ZDW sets the rough wavelength range where phase matching will allow efficient FWM to occur with a degenerate pump, actually predicting the location of the generated frequencies requires knowing the phase refractive index dependence on frequency. Converting measurements of the group velocity to estimates of the phase refractive index is not possible in general, but a method for doing so in the guidance window of a hollow-core fiber will be put forth.

CHAPTER VIII

MODEL FOR DISPERSION IN FLUID FILLED FIBER

As discussed in Chapter 2, the phase matching required for four-wave mixing (FWM),

$$k_1 + k_2 - 2k_3 + 2\gamma P_3 = 0, \quad (8-1)$$

is dependent on the phase refractive index, $n(\omega)$,

$$\frac{n_1(\omega_1)\omega_1}{c} + \frac{n_2(\omega_2)\omega_2}{c} - 2\frac{n_3(\omega_3)\omega_3}{c} + 2\gamma P_3 = 0, \quad (8-2)$$

with,

$$k_j = \frac{n_j(\omega_j)\omega_j}{c}. \quad (8-3)$$

Measuring the phase refractive index profile of the guidance window would then allow predictions of what, if any, frequencies entangled photon pairs would be generated at for a given pump frequency. But accurately measuring the phase refractive index of the system is non-trivial [66].

By contrast, the group refractive index profile of the fiber's guidance window is straight forward to learn from the group velocity profile polynomial fit found from the Mach-Zehnder interferometer group velocity measurements of the previous chapter:

$$n_g(\omega) = \frac{c}{v_g(\omega)}. \quad (8-4)$$

A method of converting from group refractive index measurements to phase refractive index would circumvent the issue of directly measuring the phase refractive index. At a

first glance, this should be trivial to do as the group and phase refractive indices are related by a single equation,

$$n_g(\omega) = n_p(\omega) + \omega \frac{\partial n_p(\omega)}{\partial \omega}, \quad (8-5)$$

where the subscript explicitly labels the phase refractive index. However, the derivative in the last term of Equation 8-3 suggests a measurement of $n_g(\omega)$ cannot be used to uniquely determine $n_p(\omega)$ in a general case [66]. This chapter focuses on particular cases where an estimate for the phase refractive index can be extracted from group refractive index measurements and how doing so can be used to predict the phase matching conditions necessary for degenerate FWM.

8.1 Modeling Phase Refractive Index

The impediment placed by the derivative in the last term of Equation 8-5 can be circumnavigated in the particular case where the group refractive index and the phase refractive index may both be accurately modeled as polynomials. Under a polynomial approximation, the phase refractive index may be described as,

$$n_p(\omega) = A + B\omega + C\omega^2 + \dots, \quad (8-6)$$

where the terms A, B, C, \dots are unknown constants. The derivative of Equation 8-6 then takes the form,

$$\frac{\partial n_p(\omega)}{\partial \omega} = B + 2C\omega + \dots, \quad (8-7)$$

such that

$$\begin{aligned}
n_g(\omega) &= A + B\omega + C\omega^2 + \dots + \omega[B + 2B\omega^2 + \dots] \\
&= A + 2B\omega + 3C\omega^2 + \dots \\
&= \tilde{A} + \tilde{B}\omega + \tilde{C}\omega^2 + \dots
\end{aligned}
\tag{8-8}$$

Because the constants in both polynomial representations are related to each other by a simple scaling term set by the power of the polynomial, determining the values of the constants $\tilde{A}, \tilde{B}, \tilde{C}, \dots$ is sufficient to determine the values of the constants A, B, C, \dots

Using this method with the group velocity measurements at 80 atm and 95 atm from Chapter 7, the phase refractive index estimated curve was found. From that curve, frequencies that satisfied phase matching and energy conservation over a range of pump wavelengths could be determined. These curves are shown in Figure 8.1.

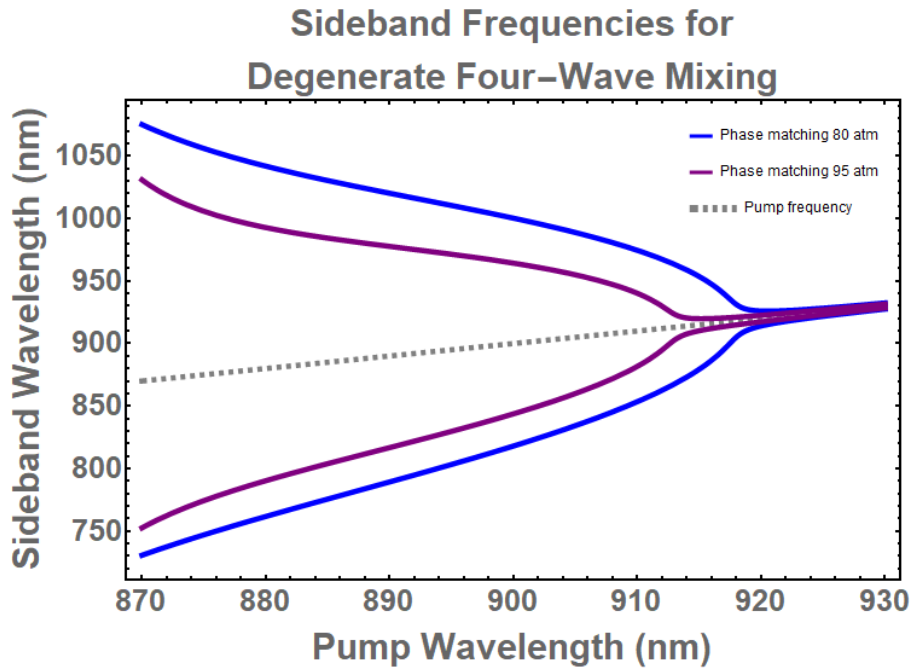


Figure 8.1. Predicted Phase Matching Curves. Plots of the predicted wavelengths of sideband created by degenerate FWM from the measured group velocities of the guidance window at 2 pressures of supercritical xenon.

At wavelengths longer than the ZDW, phase matching demands the sideband frequencies of the FWM process by quite close to the pump frequency, as is seen for longer wavelengths in Figure 8.1. Once the pump wavelength is just shorter than the ZDW, the FWM sidebands rapidly diverge from the pump. The ZDW of the fiber under 80 atm of xenon is shown to be at a longer wavelength than the ZDW of the fiber under 95 atm of xenon, as expected for the dispersion curve and guidance window shifting with increased xenon density.

It should be noted that the guidance window of the fiber at these pressures ranges from roughly 775 nm to 950 nm and predicted phase matching beyond those wavelengths is unphysical.

8.2 Dispersion Pressure Dependence

In addition to being able to predict the phase refractive index from group refractive index measurements, it would be useful to have some way of estimating how this phase refractive index curve would change with xenon pressure. But as was mentioned in the previous chapter, the scalar model does not produce accurate predictions for the ZDW or any other feature of the dispersion curve. This is because that model only accounts for changes to the waveguide caused by the modifying the photonic crystal with the density of the filling fluid. A model which incorporates the changing material dispersion contribution of the xenon fluid to the total dispersion of the system can reproduce the observed changes in the dispersion profile.

This may be most easily demonstrated with a simple 2nd-order polynomial toy model. For concreteness, let the guidance window of the vacuum filled fiber initially be

located between 950nm (1.8 PHz in angular frequency) and 1150nm (1.4 PHz in angular frequency)

The phase refractive index of xenon over a large range in wavelengths is accurately described by the Sellmeier dispersion Equation 4-5 and plotted in the guidance window in Figure 8.2. Over the range of the fiber's guidance window, however, the xenon's material phase refractive index may be approximated by a 2nd order polynomial.

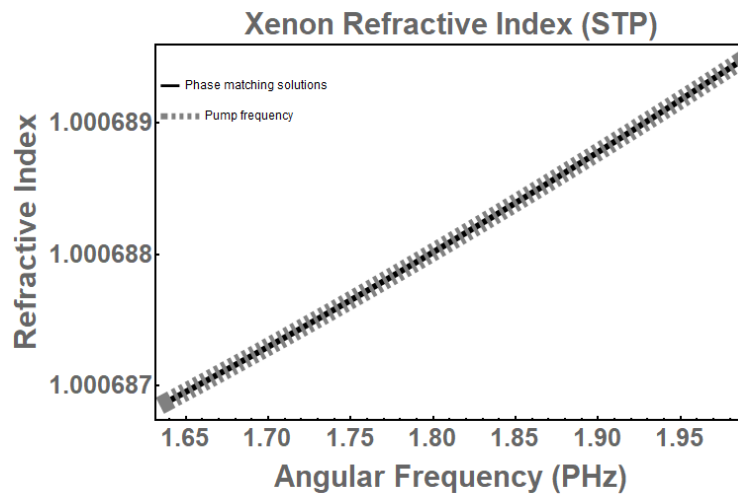


Figure 8.2. Quadratic Fit to Sellmeier. A plot of a 2nd order fit to the Sellmeier dispersion curve over the frequencies of the toy model's guidance window to demonstrate the validity of using a polynomial approximation.

The normal dispersion of bulk xenon manifests in the positive slope of the phase refractive index curve as a function of frequency.

For the sake of this toy model, let me assume the group velocity in the guidance window of the evacuated fiber may also be modeled by a 2nd-order polynomial, where the group velocity resides in the center of the guidance window. The corresponding group refractive index then has a minimum value at the center of the window as well. This is

shown in Figure 8.3. The phase refractive index of the system is found as described above and the waveguide contribution to the phase refractive index determined from,

$$\tilde{n}(\omega) = n_M(\omega) + \Delta n_{WG}(\omega), \quad (8-9)$$

where the material contribution $n_M(\omega) = 1$ for all frequencies because the fiber is in vacuum. The waveguide contribution is plotted in Figure 8.3, and shows anomalous dispersion.

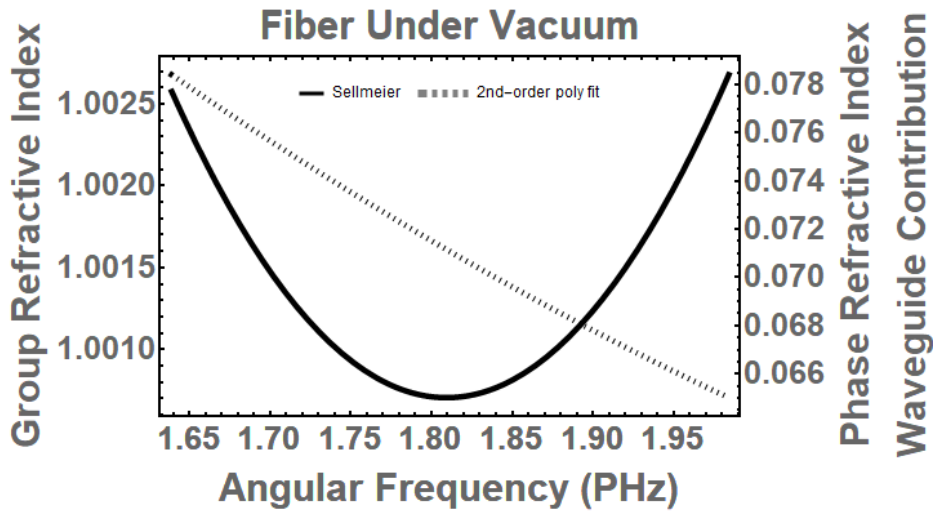


Figure 8.3. Group and Phase Refractive Index of Toy Model: The plotted group refractive index and waveguide contribution to the phase refractive index for the HC-PBG fiber in the simple model.

If the fiber is now filled at room temperature to 1 atm of xenon, the material and waveguide dispersions from Equation 8-9 combine to give a total effective phase refractive index for the system. At 1 atm of xenon, the group velocity of this system closely matches that of the vacuum filled system, with a vertical offset caused by the light now traveling at a slower speed relative to when the fiber was under vacuum. This is shown in Figure 8.4.

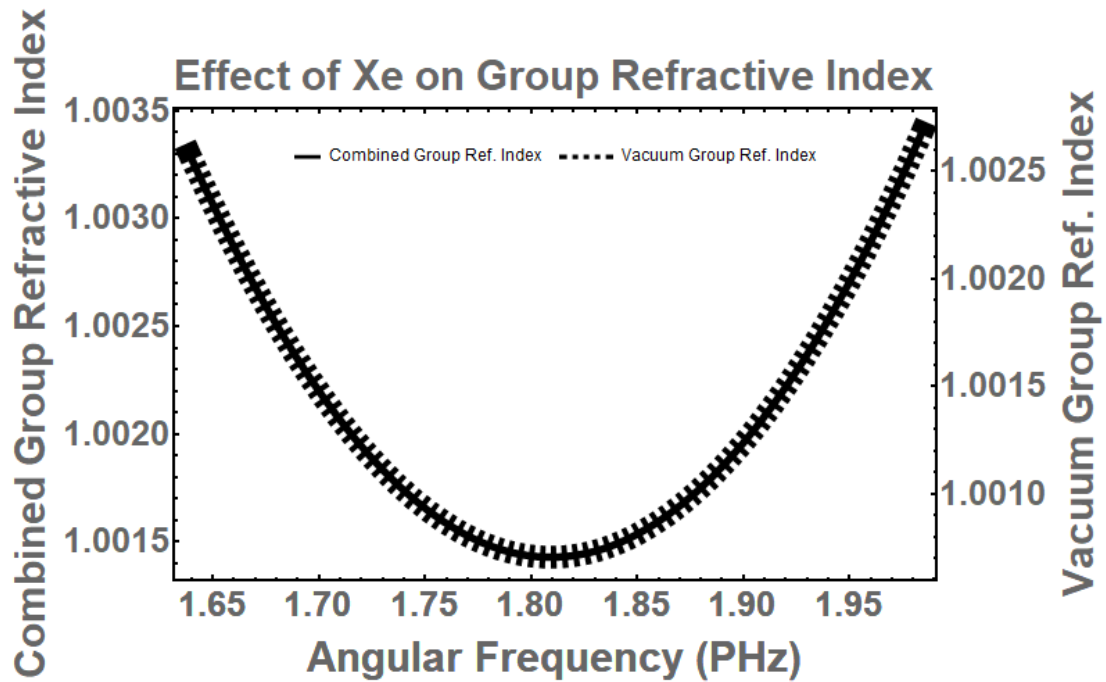


Figure 8.4. Combined Group Refractive Index at 1 atm: A plot of the group refractive index created by the photonic crystal’s limits on the guidance window and the composite system with the HC-PBG’s core filled with 1 atm of xenon. The overlap of the 2 curves highlights the negligible effect the material dispersion has on the composite system at low pressures.

Now, say the fiber is filled to 70 atm of xenon. From the scalar model of Chapter 6, this shifts the short wavelength edge of the guidance window to 750 nm. The waveguide’s contribution to the phase refractive index is simply shifted by the same mechanism that shifts the edges of the guidance window. In addition, the increased density of xenon changes the material refractive index of the core, as now it is based on a subsection of the Sellmeier at shorter wavelengths and at greater density. By scaling the Sellmeier to the appropriate density and fitting a 2nd-order polynomial to the new guidance window wavelengths, the materials phase refractive index may be found.

Combining the material refractive index with the waveguide contribution gives the total phase refractive index of the system.

Solving for the group refractive index, the minimum value is seen to no longer reside in the center of the guidance window, but rather to have been shifted to longer wavelengths by the addition of the material dispersion of the core.

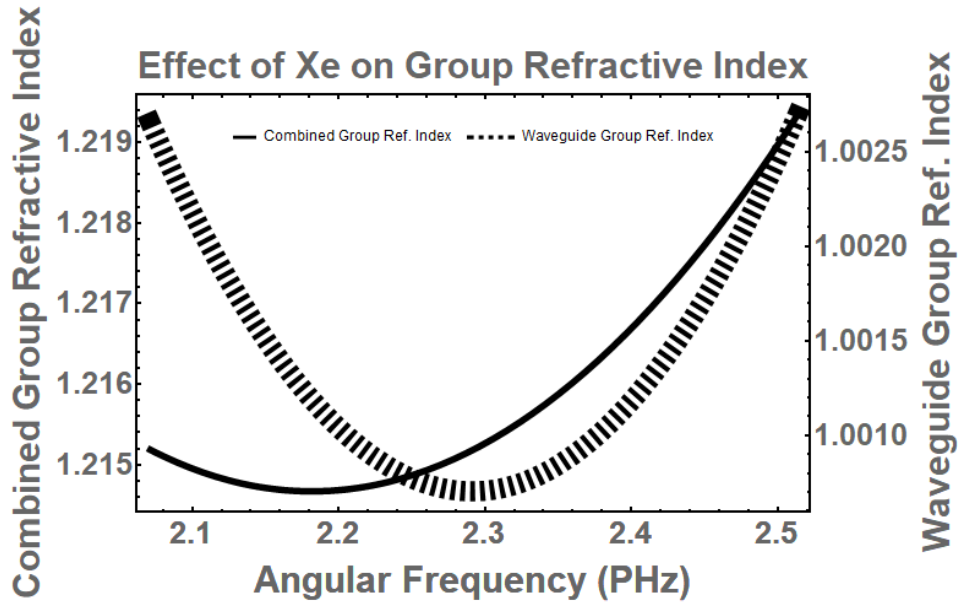


Figure 8.5. Combined Group Refractive Index at 70 atm: A plot of the group refractive index created by the photonic crystal’s limits on the guidance window and the composite system with the HC-PBG’s core filled with 70 atm of xenon. The mismatch of the 2 curves highlights the substantial amount the material dispersion contributes to the composite system and demonstrates the asymmetry seen in the experimental measurements of $n_g(\omega)$.

Using this model, the approximate location of the ZDW at pressures of xenon may be modeled and used to determine appropriate pressures of xenon for achieving phase matching with a given pump wavelength.

8.3 More Work to be Done

The polynomial model used above relies on a polynomial fit to the measured group refractive index. The relative scarcity of recorded group refractive indices in the guidance window and the associated error bars from the previous chapter limits the quality of this fit. This is especially true for records at lower pressures of xenon, when even fewer group refractive index measurements were performed.

Because of this limitation, the model was only able to give estimated regions for the generation of sidebands. A more complete mapping of the guidance window's group refractive index may improve this technique.

CHAPTER IX

ENTANGLED PHOTON GENERATION BY FOUR-WAVE-MIXING

Chapters 7 and 8 demonstrated that the guidance window and dispersion profile of xenon filled Hollow-core photonic bandgap (HC-PBG) fiber could be modified by altering the linear refractive index of the filling fluid. Furthermore, both processes could be modeled in order to predict what wavelengths would be guided by the fiber and what wavelengths would achieve phase matching in spontaneously generating sidebands from degenerate four-wave mixing (FWM). But to be a source of tunable, entangled photon pairs, the xenon filled fiber needed to produce said photon pairs. This chapter describes the generation, observation, and verification of those sidebands.

9.1 Experimental Setup

Using the models and measurements described in the previous chapters, a filling pressure of 1250 psi (85 atm) was chosen for the xenon. This shifted the guidance window of the fiber to 775-965 nm, moved the zero dispersion wavelength (ZDW) to 920 nm, and gave the core of the fiber a nonlinear refractive index of $n_2 = \frac{2.0 \times 10^{-16} \text{ cm}^2}{\text{W}}$ (comparable to that of fused silica) [18]. A pulsed 80 MHz Ti:sapphire laser at wavelengths just under the ZDW and pulse duration of around 10 ps was coupled into a 4 meter xenon filled section of the HC-PBG fiber. The duration of the pulse was inferred from visibility measurements of the 1st-order correlation of the beam, assuming a Gaussian limit. A rotatable half-wave plate and polarizing beamsplitter were used to control both the polarization and total power of light being coupled into the xenon fiber.

The light transmitted by the fiber was then passed through another polarizing beamsplitter aligned with the first and imaged onto a pinhole, which helped to remove Raman generated light from any excited surface and lattice modes. After the pinhole, the remaining light was re-collimated, filtered to remove the pump, and recorded with a liquid nitrogen cooled spectrometer, as shown in Figure 9.1. A flip mirror allowed a white light source to be coupled through the fiber and used to align the output of the xenon fiber with the spectrometer.

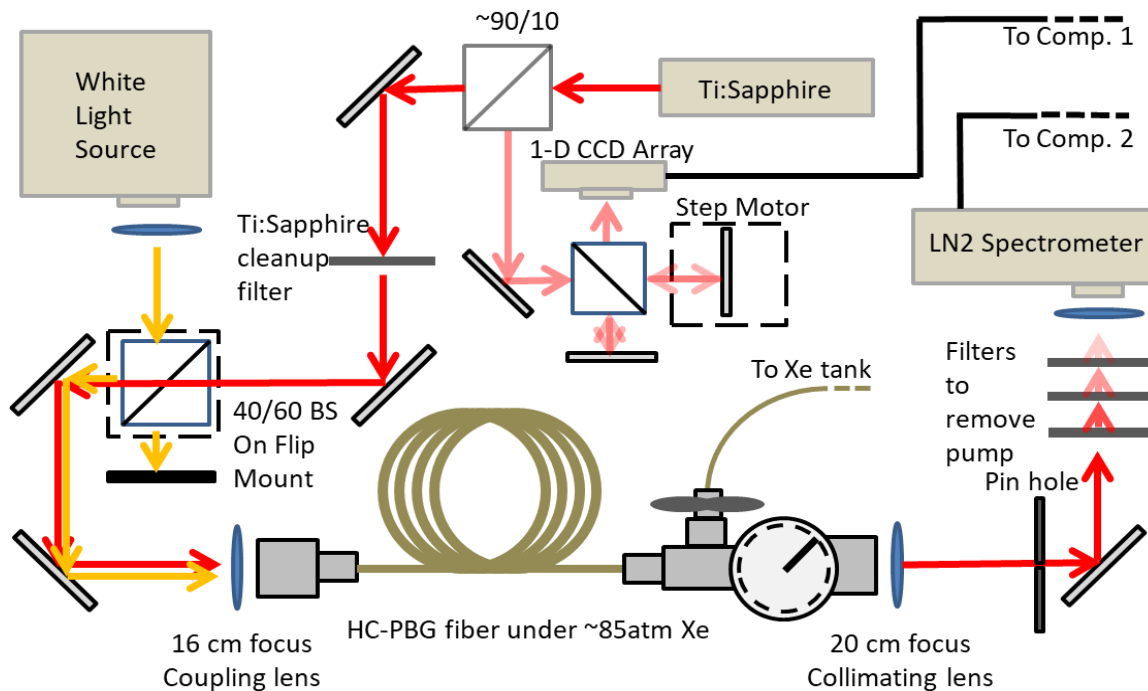


Figure 9.1. Sideband Spectrum Setup: The diagram for observing the generation of sidebands from a Ti:Sapphire pump pulse on a spectrometer. A Mach-Zehnder interferometer was used to verify the pulse duration and a White Light Source to optimize transmission of light from the xenon filled fiber to the spectrometer.

9.2 Observations of Sidebands

The filters used to block the pump wavelength from saturating the spectrometer also limited the spectrometer to only being sensitive to wavelengths longer or shorter

than the pump wavelength for any given recording. Two of these measurements are combined and shown in Figure 9.2, showcasing the detected sidebands at 890 nm and 945 nm for the 914.4 nm pump. Diminished sensitivity of the spectrometer at longer wavelengths largely account for the reduced count rates for the longer wavelength sideband.

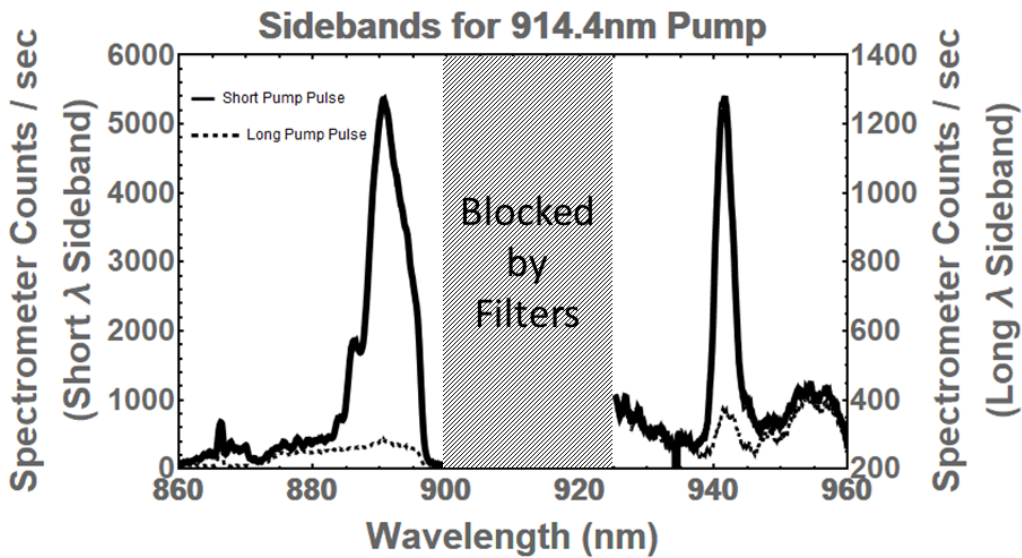


Figure 9.2. Sideband Peak Pump Power Dependence: The sideband peaks in the spectrum for short and long pulses with average power held constant are shown, demonstrating the sideband dependence on peak pump power.

In addition to detecting photons generated in the predicted sideband frequencies of the system, additional photons were detected in these measurements. The small, broad peak at 955 nm in Figure 9.2 is one such example. This peak corresponds to a peak in the Raman spectrum of fused silica for a 914 nm pump laser, so it was believed that some amount of laser-fused silica interactions were occurring. Verifying that the photons at the sideband wavelengths came from a mechanism like FWM and not Raman scattering was done by varying the pulse duration of the pump.

The sideband gain from FWM is quadratically dependent on the peak power of the pump laser, while Raman scattering only depend on the average power of the pump. To verify that the signals being observed on the LN2 spectrometer were from a source depending on the peak power of the pump laser, 2 spectrum measurements were recorded for every pump wavelength, power, and polarization. The first measurement used a short 10-15 ps pulse duration while the second had a much longer (100-300 ps) pulse duration. The average pump power remained constant for both pulse durations, so the longer pump pulses had a much lower peak power. This caused any signal from a process dependent on peak power to be greatly diminished.

By comparing the measurements with 2 different pulse durations, it was possible to verify the sideband peaks were dependent on the peak power of the pump pulses while the Raman peaks intensity depended on the average pump power. Improved coupling of the pump into the fiber could help remove the remaining Raman scattering.

9.3 Energy Conservation

Energy conservation must hold in FWM. Coupled with the phase energy requirement, these two rules place strong constraints on the parameters of a system needed to generate observable sidebands. Based on the dispersion models and measurements described in Chapters 7-8 and the guidance window range from Chapter 6, it was expected that the energy and phase conversation constraints would define different sideband wavelengths for different pump wavelengths around the ZDW.

In particular, as the pump wavelength approached the ZDW from the short wavelength side, it was expected that the difference in wavelength between the pump and

both sidebands would decrease in such a way that the short wavelength sideband (idler) would increase at a faster rate than the pump and the long wavelength sideband (signal) would decrease as the pump wavelength increased.

To observe this effect, the pump wavelength was tuned over a range of wavelengths from 911.1 nm to 915.5 nm for input polarizations along both the fast and slow axes of the fiber. The sideband wavelengths intensities were recorded by the LN₂ spectrometer. The resulting transition of the observed sideband peaks are shown in Figure 9.3.

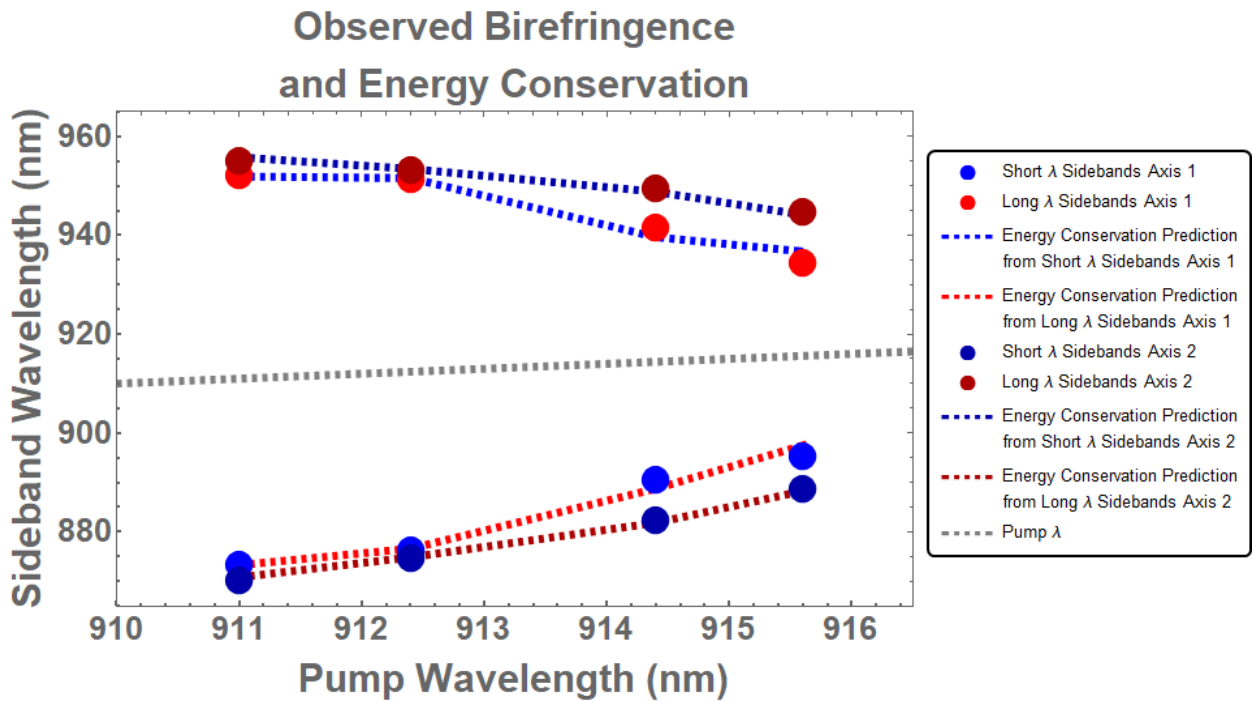


Figure 9.3. Observed Birefringence and Energy Conservation: Plot of the measured peak intensities of sidebands generated at multiple pump wavelengths and along both axes of the xenon filled fiber. For a given polarization and pump wavelength, the sideband peaks obey energy conservation. Over multiple pump wavelengths, the peaks also follow the predicted slopes of light from degenerate four-wave mixing.

The sideband wavelengths move as expected for light produced by degenerate FWM. As the pump wavelength is increased, the shorter wavelength idler increases at a faster rate while the longer wavelength signal decreases.

The slight birefringence of the fiber, described in Chapter 7, was also observed, where the different dispersion profiles of the axes of the fiber resulted in the generation of sidebands at slightly different wavelengths. However, the fiber was only moderately polarization maintaining, so additional work would need to be done to make use of this birefringence to expand the tunability of the system even further.

Using the pump frequency and the frequency of one of the sidebands, predictions for the location of the second sideband could be made using conservation of energy. These predictions are shown in Figure 9.2, and the overlap between predictions and measured intensity peaks verifies that the process generating the sidebands obeys energy conservation.

Comparing these measured results from the model put forth in Chapter 8 and shown in Figure 8.1, the sideband wavelengths from the experimental results at 85 atm of xenon fall between the predicted wavelengths for 80 atm and 95 atm, as shown in Figure 9.4. Limitations of the model are apparent in the differences between the slopes of the predicted phase matching curves and the experimentally observed sideband wavelengths. Additional work to improve the phase matching model at arbitrary pressures still needs to be performed, but the measurement of sideband wavelengths between the two theoretical curves is an encouraging indicator that the model can capture the overarching structure of the system.

Comparing Model and Measurement of Sidebands

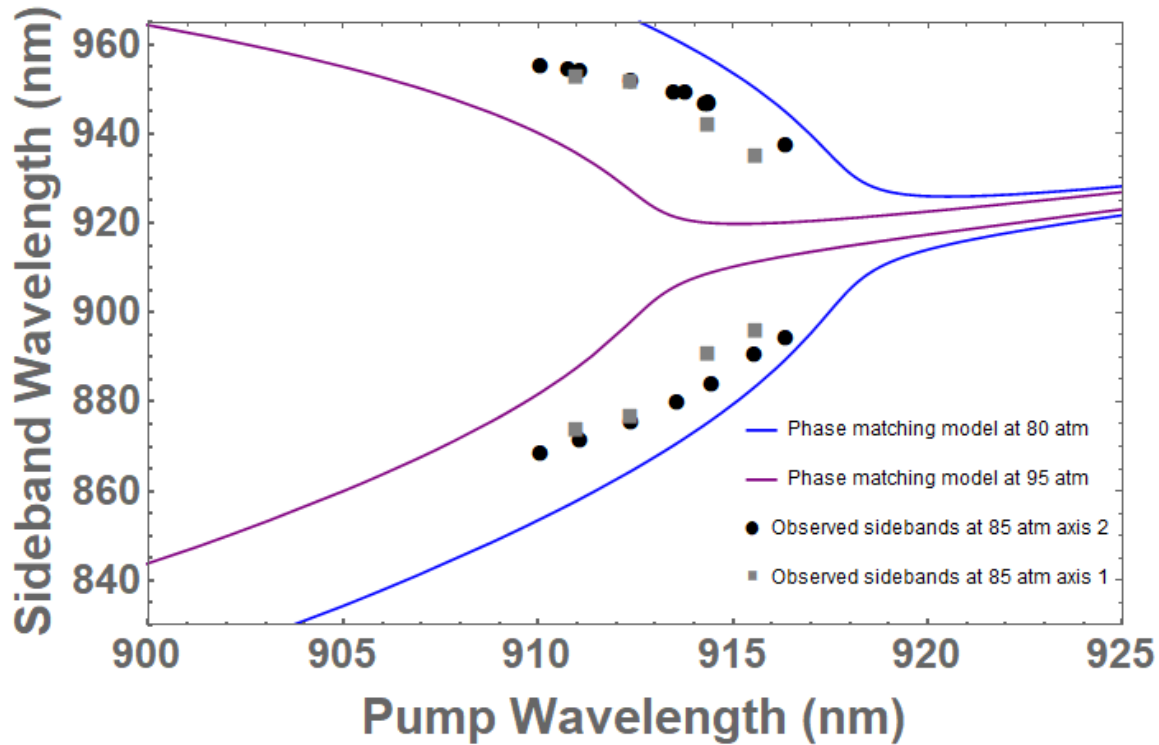


Figure 9.4. Comparing Measured Sideband Wavelengths to Predictions: Plot of measured sideband wavelengths for both axes of the fiber at 85 atm falling between predicted sideband wavelengths for pressures of 80 and 95 atm.

9.4 Seeding

In the above experiments, spontaneous FWM served to generate the initial sideband photons. One of the sidebands could be initially seeded, however, to produce an amplified signal in the other sideband. This was done using a weak continuous wave (CW) diode laser centered at 882 nm, which overlapped the sideband gain range of the xenon filled fiber when the pump was at 914.3 nm. The resulting gain in the sideband spectrum at 949 nm is shown in Figure 9.5 and demonstrates the amplified growth of wavelengths which satisfy energy conservation with the CW seed and pump.

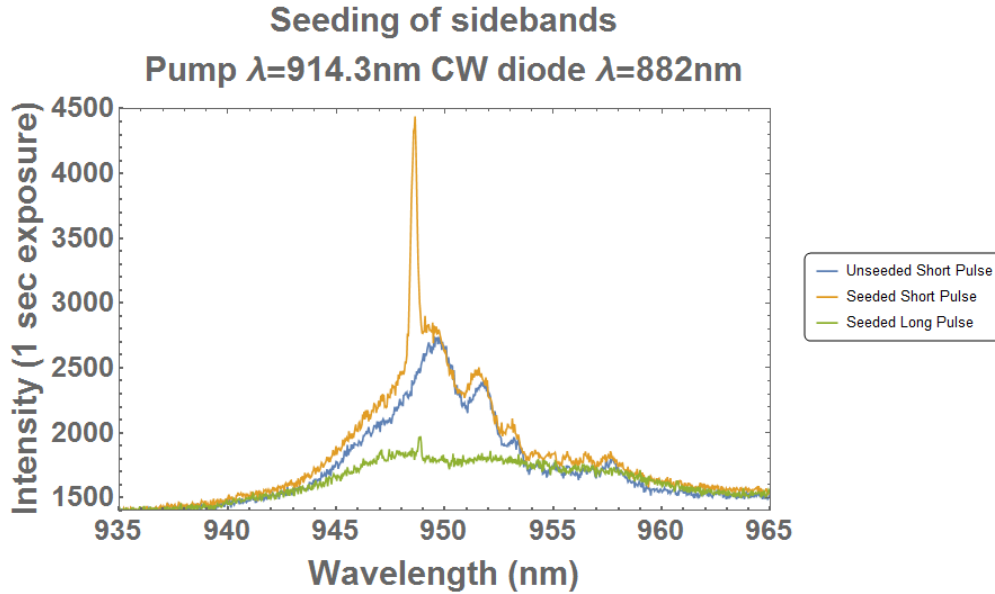


Figure 9.5. Seeded Amplification: Measurement of the seeded amplification from a CW diode laser co-coupled into the fiber within the short wavelength sideband spectrum. A fringe pattern from the filters used to block the pump from entering the spectrometer is also visible on the spontaneous gain spectrum.

While further work was not performed in this seeded regime, this demonstrated the possibility of using the prototype system to convert single photons from one sideband wavelength to the other [13].

9.5 Single Photon Statistics Setup

When generating photons by spontaneous degenerate FWM, a key feature is that they are generated in pairs. For every photon produced in the signal wavelengths, a corresponding photon should be produced in the idler wavelengths. While the LN_2 spectrometer could measure the intensity of the sidebands and verify they obeyed energy conservation and pump peak power dependence, it was not able to verify a correlation in generation of the photons in the sidebands.

To measure this correlation, the experiment was modified to remove the LN₂ spectrometer and include avalanche photodiodes (APDs) capable of detecting single photons.

The pump wavelength was fixed at 912 nm, with sideband wavelengths observed at 870 nm and 958 nm. For the following work, I'll call the short wavelength sideband photons the idler and the long wavelength sideband photons the signal. Prisms were added to the experimental setup after the pinhole to separate the signal and idler wavelengths from the pump, filters were installed to remove the remaining pump light, and multimode, solid-core fibers were used to guide the signal and idler photons to single photon sensitive APDs, as shown in Figure 9.6.

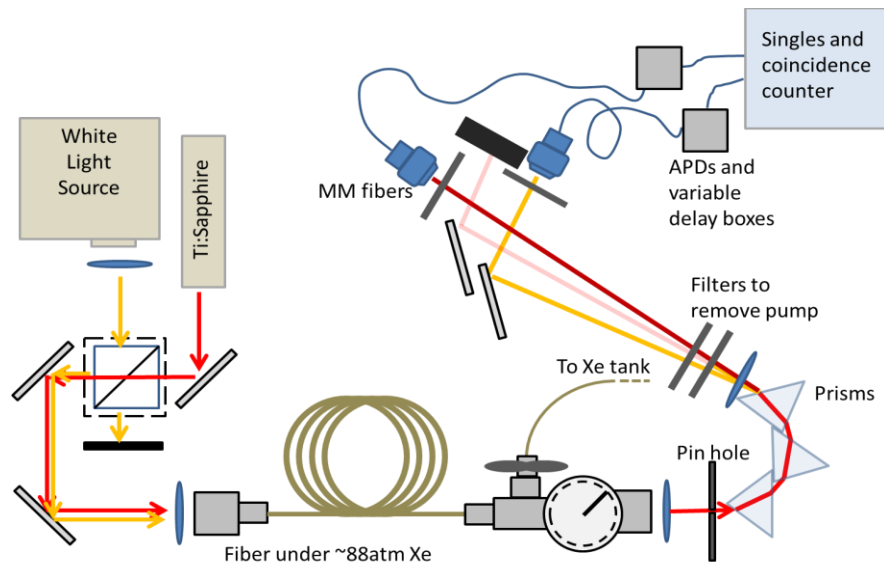


Figure 9.6. Correlations Setup: The experimental design for measuring correlations between photons in the sidebands.

To initially align the system, the white light source (WLS) from Chapters 6-7 was coupled into the HC-PBG and the classical fields at the wavelengths of the generated

sidebands used to optimize detection. Once optimized, the WLS was removed and the pulsed Ti:sapphire pump used to generate sidebands at the appropriate wavelengths.

Once a photon was detected by the APD, an electronic signal was sent by the APD via a BNC cable to a field-programmable gate array (FPGA) coded for coincidence counting. The FPGA had a measured coincidence window of 1.36 ns, long enough that all photons from a 10 ps pulse would be detected in the same window, but short enough that the 12.5 ns separated pump pulses could be distinguished. Delay boxes were placed in the BNC cable line to allow the signal from the APD to be delayed up to 73.5 ns in .5 ns increments.

9.6 Correlations vs Delay

Singles count rates of the APDs ranged from a ~100,000 counts/sec to ~1,000,000 counts/sec, meaning the average number of photons detected from a single pulse was less than 1. Operating in this regime kept the dead time of the APDs from being of concern. Using the delay boxes on the BNC lines between the APDs and FPGA, coincidence counts could be measured comparing different arrival times between the signal and idler photons.

The correlations from the coupled generation of signal and idler sidebands would be reflected in a large number of coincidence measurements when APD detections from the same pulse were overlapped in the coincidence window of the FPGA. When the APD detections from the same pulse were delayed relative to one another such that they did not fall into the FPGA coincidence window, this enhancement in detected coincidences should not be detected. Measurements of coincidences were taken for relative delays

between the APD detectors ranging from -30 ns to +30 ns, as shown in Figure 9.7. The delay at 0 ns corresponded to an overlap of detections from the same pulse.

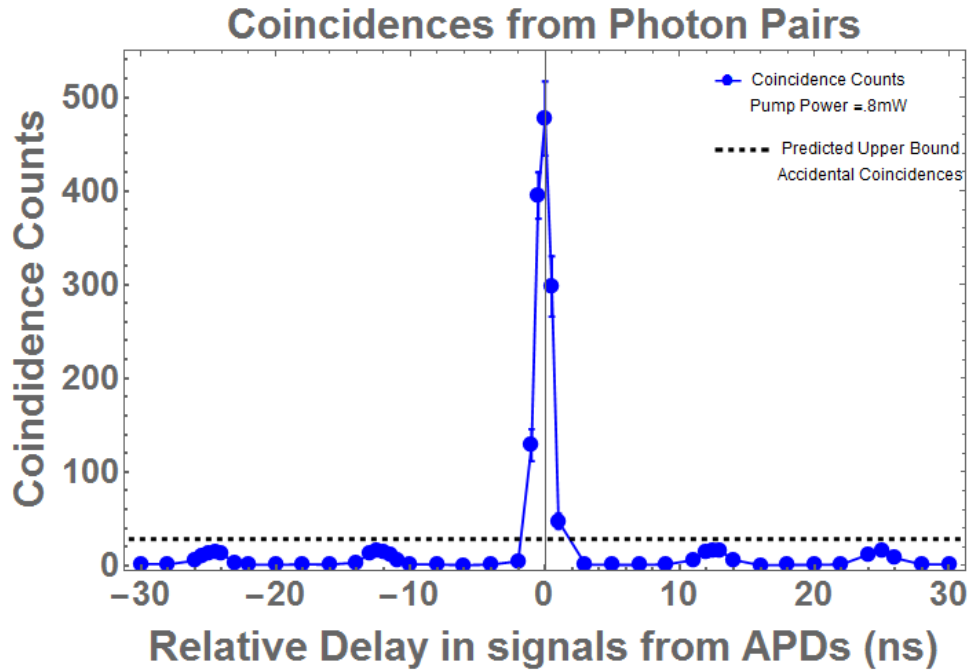


Figure 9.7. Coincidence as a Function of Delay: A plot of the coincidence counts between the APDs as a function of delay. The strong peak at 0 ns delay comes from the correlations present in the FWM generated sidebands. The smaller peaks at other delays correspond to accidental counts when detections from 2 different pulse events are overlapped on the FPGA.

The number of detected coincidences is never expected to reach zero. Accidental coincidence measurements dependent on the statistics of the single count rates were expected for all time delays, with an upper bound for these accidental coincidence set as shown in the following section.

9.7 Calculating the Accidental Coincidences

We can approximate light from thermal sources and the electronic dark counts of the APDs as being continuous [32]. Without intensities that vary with time, calculating

the expected rate of accidental coincidence counts is straight forward under the assumptions that detections are independent and follow Poisson statistics.

Given the detected singles rates, the rate of accidental coincidences will be the rate of singles from each APD multiplied by the coincidence window of the FPGA,

$$N_{acc} = N_s \times N_i \times T_w, \quad (9-1)$$

where N_s is the number of counts/sec detected by the signal APD, N_i is the number of counts/sec detected by the idler APD, and T_w is the coincidence window. For example, if $N_s = N_i = 1000/\text{sec}$ and $T_w = 1 \text{ ns}$,

$$N_{acc} = N_s \times N_i \times T_w = \frac{1000 \times 1000 \times 10^{-9}}{\text{sec}} = \frac{.001}{\text{sec}}. \quad (9-2)$$

In the case of pulsed input, this simple equation no longer applies because the probability of detection varies with the amplitude of the incoming light. Under the assumption that the pulses are much shorter than the detection window, there is no need to worry about the shape of each pulse. In this case the number of accidental coincidences detected per second will depend on the pulse rate of the source, f_{rep} :

$$N_{acc} = \frac{N_s \times N_i}{f_{rep}}. \quad (9-3)$$

If $N_s = N_i = 1000/\text{sec}$ and $f_{rep} = \frac{100,000}{\text{sec}}$, the average expected accidental rate would be,

$$N_{acc} = \frac{N_s \times N_i}{f_{rep}} = \frac{1000 \times 1000}{100,000 \text{ sec}} = \frac{1}{\text{sec}}. \quad (9-4)$$

Realistically, the detections from the APDs in the experiment will come from both pulsed and continuous sources, so the total accidental count number will be a combination of Equations 9-1 and 9-3:

$$N_{acc} = \frac{N_s^{pulse} \times N_i^{pulse}}{f_{rep}} + N_s^{cont} \times N_i^{cont} \times T_w. \quad (9-5)$$

Without conducting measurements to determine the ratio of detected photons coming from pulsed and continuous sources, an upper bound may be found for the accidental coincidence count by assuming all detected photons are from either a pulsed or continuous source, calculating the expected accidental count total, and keeping the maximum value:

$$N_{acc}^{upper\ bound} = \text{Max} \begin{cases} \frac{N_s \times N_i}{f_{rep}}, & \text{pulsed source} \\ N_s \times N_i \times T_w, & \text{continuous source.} \end{cases} \quad (9-6)$$

This is the upper bound on accidentals shown on Figure 9.7 as the horizontal dashed line. The coincidence rate for delays $|\tau| > 1$ ns falls under this upper bound, indicating that those counts may be described as accidentals. When the detection signals from the same pulse are optimally overlapped in the detection window of the FPGA ($\tau \approx 0$ ns), the detected coincidence rate is over 10 times greater than this upper bound, indicating some process is generating correlated photons at the sideband wavelengths of the degenerate FWM process in the fiber.

In addition to observing the expected correlations between the signal and idler photons at zero relative time delay, measurements of the coincidence rate as a function of pump power were also performed.

The quadratic growth in coincidence counts is shown in Figure 9.8, and agrees with the expected gain from degenerate FWM first shown in Chapter 2.

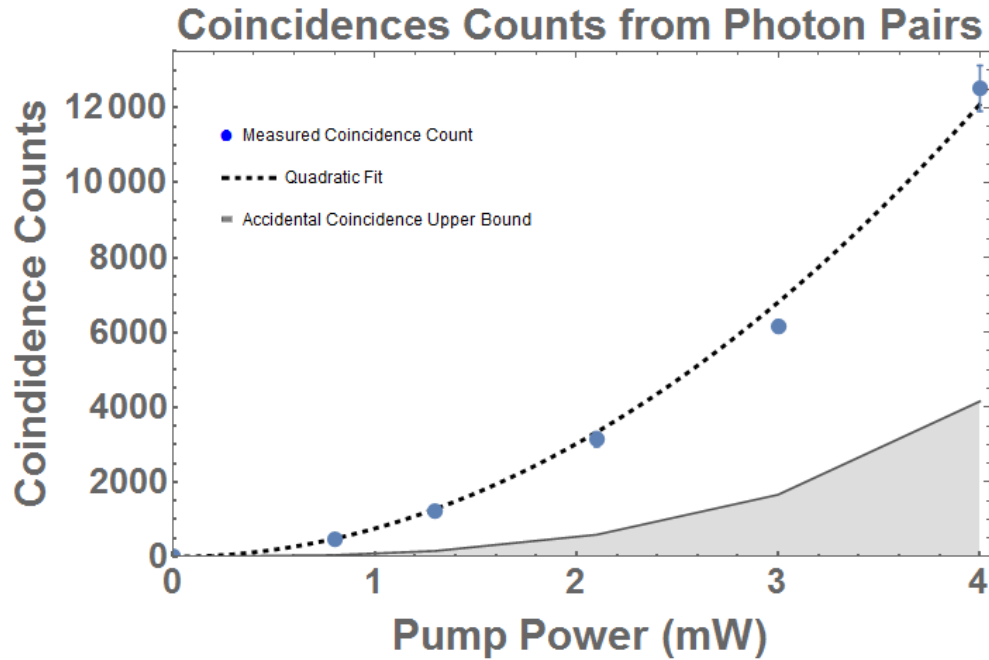


Figure 9.8. Quadratic Coincidence with Power: A plot of the coincidence count rate as a function of power showing the quadratic nature of both the coincidence counts and the upper bound on the accidental coincidences.

9.8 Second-Order Correlations

The generation of correlated photon pairs by spontaneous degenerate FWM is a non-classical phenomenon, as discussed in Chapter 2. To support the claim that the photons being generated in the xenon filled fiber are entangled and not just classically correlated, a $g^{(2)}$ measurement of the intensity correlations in one of the sidebands was performed. As discussed in Chapter 2, a $g^{(2)} < 1$ would violate the classical inequality and verify that some amount of entanglement existed between the generated photons.

To measure $g^{(2)}$, a 50:50 beamsplitter was used to split the photons from the signal wavelengths and a 3rd multimode fiber and APD added to the detection scheme. An additional delay line was also included before the FPGA as shown in Figure 9.9.

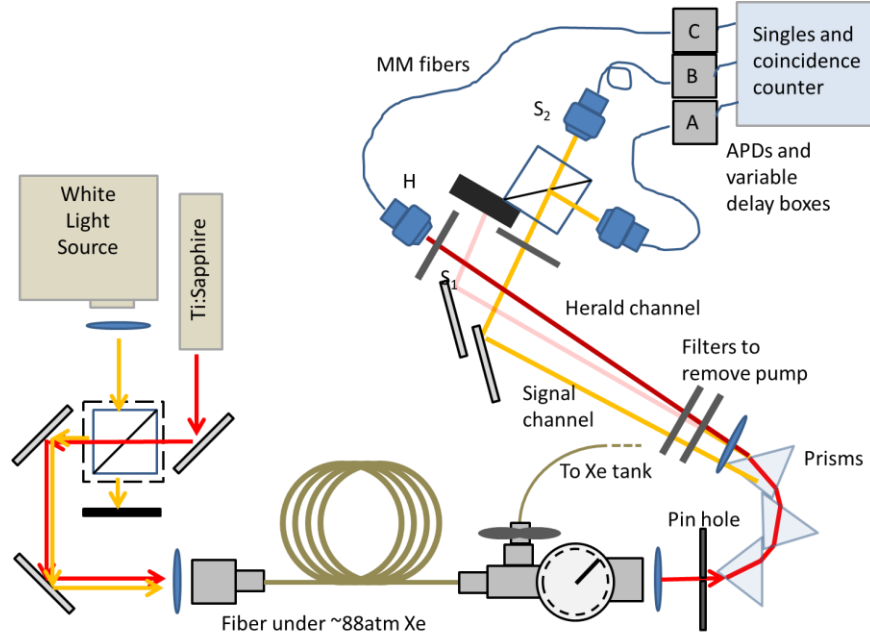


Figure 9.9. Experimental Setup for 2nd-Order Correlations: A diagram of the modified correlation experiment, now with a third APD for heralded $g^{(2)}$ of the signal channel.

The heralded $g^{(2)}$ was measured using detections from the idler wavelength APD as a herald. As described in Chapter 2,

$$g^{(2)} = \frac{N_{ABC}N_C}{N_{AC}N_{BC}}. \quad (9-7)$$

In an ideal case with no loss, no noise, and no time delay between the overlap of detection signals from the three APDs, the two photons generated by degenerate FWM should never be detected at all three detectors. So with $N_{ABC} = 0$, $g^{(2)} = 0$. As soon as a time delay is added to the system, the possibility of coincidence counts between S_1 and S_2

will return, as now a coincidence measurements can occur from photons from multiple pairs.

Measurements of $g^{(2)}$ were performed for two different delay settings with a pump average power of 5 mW and pulse width of 13.5 ps. In the first instance, the delay box settings for all three APDs were set such that the detections from the same pump pulse were overlapped on the FPGA (0 ns delay). In the second instance, the delay boxes were used to overlap three different pulses on the FPGA (+/-12.5 ns delay). One hundred recordings of counts each over a 10 second interval were performed and the average values measured for the count rates shown below. A third recording with the pump laser blocked was also performed to collect dark count and electronic count statistics to remove from the raw values recorded in the first measurements.

Table 9.1. FPGA Recordings for 2nd-Order Correlations: The detected number of photons and coincidences for determining $g^{(2)}$ values for 2 different time delays.

	N_A	N_{ABC}	N_{AB}	N_{AC}
$\tau = 0$	2,296,270 $\pm 93,245$	56.3 ± 8.5	20,295.2 ± 1110.7	17,847.8 ± 960.0
$\tau = \pm 12.5\text{ns}$	2,24,7030 $\pm 100,418$	4.4 ± 2.0	2670.4 ± 220.4	2350.5 ± 190.8

The resulting 2nd-order coherence values are:

$$g^{(2)}(\tau = 0 \text{ ns}) = .36^{+.11}_{-.10}$$

$$g^{(2)}(\tau = \pm 12.5 \text{ ns}) = 1.57^{+1.27}_{-.87}$$

Lower values of $g^{(2)}(\tau = 0\text{ns})$ were observed with lower pump powers, but because of the very low rates of heralded coincidences in the $\tau = \pm 12.5\text{ ns}$ design, insufficient statistics for $g^{(2)}(\tau = \pm 12.5\text{ ns})$ were recorded for those lower powers, While additional measurements should be performed to reduce the error bars on the $g^{(2)}$ values, $g^{(2)} < 1$ for $\tau = 0\text{ ns}$ time delay demonstrates that the light being produced by the degenerate FWM is non-classical, indicative of its makeup by pairs of single photons.

CHAPTER X

CONCLUDING REMARKS

This dissertation described a prototype source of tunable entangled photons by combining a hollow-core photonic bandgap (HC-PBG) fiber with a noble supercritical fluid. By changing the density of the fluid filling the fiber, the guidance and dispersion properties of the system could be optimized for desired phase matching conditions to produce photon pairs by degenerate four-wave mixing. The ability to tune the dispersion profile of the fiber, in particular, opens another degree of freedom to generating entangled photons. By proper choices of pump laser wavelength and xenon density in the system, the wavelengths and wavelength separations of the entangled photon pairs can be chosen.

This system can serve as a heralded source for single photons with a range of central wavelengths. At a given xenon pressure, tuning the pump laser allows for a range of sideband wavelengths to be accessed within the guidance window of the fiber. And while not experimentally shown in this dissertation, changing to a new pressure of xenon in the fiber opens up new wavelengths for the sidebands.

Applications that need control over the central wavelengths of both photons generated by the four-wave mixing process may find this system especially attractive, as the extra degree of freedom provided by a tunable dispersion profile allows the wavelengths of each sideband to be controlled by proper control over the xenon pressure and pump wavelength.

The use of a material without strong Raman gain should also not be forgotten, as this prototype has the possibility of providing a near-ideal source of entanglement without contamination from Raman generated light.

After briefly situating the work in the larger historical and contemporary context, mathematical descriptions of light were explored to develop an understanding of how light interacts with matter in both linear, nonlinear, and quantum regimes. Particular focus was spent on how the interference of light fields may be used to measure properties of systems and how the nonlinear interactions of light with matter under specific conditions can give rise to entangled light and new frequencies.

After developing the foundational principles of generating entangled photons from light-matter interactions, this dissertation turned its attention to the hollow-core photonic bandgap (HC-PBG) fiber. The photonic crystal guidance mechanism was discussed and how that guidance mechanism provides an opportunity for controlling parameters of the waveguide by means of controlling the refractive index of the photonic crystal.

The last element needed to finish the groundwork for this dissertation was a fluid to fill the HC-PBG. The fluid needed to provide a high nonlinearity and a tunable refractive index while not acting as a source for undesired optical effects. Supercritical xenon was shown to achieve all these requirements thanks to its accessible supercritical region and its lack of vibrational modes.

With all the pieces needed for the prototype described, the next section discussed building the laboratory apparatuses that became the prototype source for entangled photons. The need to contain and control the xenon was realized by using liquid nitrogen

to control the density of xenon throughout a containment system. Cells that would withstand the pressures of supercritical xenon, support the HC-PBG fiber, and allow coupling of light to and from the core of the fiber were described, with a word of caution given about installing delicate fibers into cells without causing substantial damage.

With the prototype constructed, the 2nd half of the dissertation looked at experimental measurements and developed models used to profile the prototype and enable future projects to predict parameters without needing to measure them in the lab. The first experiments showed how increasing the density of xenon filling the photonic crystal of the fiber changed what wavelengths were guided by the fiber in a predictable fashion, opening the door to tuning the fiber to the desired wavelengths for generating entangled photons.

The next set of experiments looked within the guidance window of the fiber at the group velocity and group velocity dispersion profiles of the light. By use of a white light Mach-Zehnder interferometer, these parameters could be measured at different pressures of xenon and the zero dispersion wavelength found. The complication of measuring group refractive index when phase refractive index is the property which controls nonlinear four-wave mixing was raised, and a solution involving polynomial approximations was shown.

A model to describe the dispersion profile of the guidance window of HC-PBG fibers as a function of fluid density was developed, combining the ways the waveguide and material dispersion curves change with pressure. A toy model was shown to replicate the observed asymmetries in the group refractive index profile as well the change in the zero dispersion wavelength as a function of pressure.

With the prototype fully parametrized, the final section of this dissertation described the experimental observations of correlated photons created by degenerate four-wave mixing in the xenon filled fiber. Measurements of the wavelengths of the sidebands containing the correlated photons were shown to obey energy conservation over a range of pump wavelengths, and their growth was shown to be quadratically dependent on the peak pulse power. Coincidence measurements of the sidebands showed that the photons at those wavelengths were significantly correlated, and a 2nd-order coherence measurement demonstrated that the light being generated was non-classical in nature, as expected for pairs of single photons.

To achieve this prototype system, several challenges needed to be overcome. As discussed in Chapter 3, HC-PBG fibers guide light through a core defect in a photonic crystal that propagates through the length of the fiber. In addition to supporting core modes within a certain frequency band, these fibers also can support surface modes along the core walls of the fiber in the same frequency band. Certain frequencies that overlap both the core and surface modes are naturally lossy, as light from the core mode couples to the surface mode and then to leaky modes of the fiber's cladding. As the pressure of the xenon increased, the wavelengths of this overlap increase, leading to the possibility the entire guidance window is lossy due to overlap with surface modes. Special fibers designed to not have surface modes were necessary to achieve transmission of light at high pressures of xenon.

Temperature control was also a continuing challenge with this system. Especially near the critical point, changes in the temperature of xenon can have substantial effects on the density of xenon. This in turn can cause changes to the refractive index of the

xenon and scattering of light in the fiber. Care in controlling the temperature of the fiber throughout its length, but particularly at the tip where localized heating is most likely to occur from imperfect coupling, is necessary to achieve good transmission of light.

Looking forward, this project could benefit from additional work to improve efficiencies and statistics. Investigating the generation of correlated photons at multiple pressures and potentially on multiple polarization axes of the fiber are additional avenues that could be pursued. With the models developed in this dissertation, future projects with fluids and HC-PBG fiber could accurately estimate all parameters necessary for generating entangled photon pairs from degenerate FWM in the guidance window of the fiber. Finally, xenon's lack of vibrational modes was largely uninvestigated. Experiments on the potential of this type of system for generating entangled without significant Raman gain could open the door to fiber based photon pair generation close to the central frequency of the pump.

REFERENCES CITED

1. P. Shor, "Polynomial-Time Algorithms for Prime Factorization and Discrete Logarithms on a Quantum Computer," *SIAM Journal on Computing*, vol. 26, no. 5, pp. 1484-1509, 1997.
2. C. H. Bennett, G. Brassard, and N. D. Mermin, "Quantum cryptography without Bell's theorem," *Physical Review Letters*, vol. 68, no. 5, pp. 557-559, 1992.
3. J. Joo, W. J. Munro, and T. P. Spiller, "Quantum Metrology with Entangled Coherent States," *Physical Review Letters*, vol. 107, no. 8, 2011.
4. J. Aasi, J. Abadie, B. P. Abbott, R. Abbott, T. D. Abbott, M. R. Abernathy, et al. "Enhanced sensitivity of the LIGO gravitational wave detector by using squeezed states of light," *Nat Photon*, vol. 7, no. 8, pp. 613-619, 2013.
5. R. Loudon. *The quantum theory of light*. 3rd ed. New York, Oxford University Press, 2000.
6. M. D. Eisaman, J. Fan, A. Migdall, and S. V. Polyakov, "Invited Review Article: Single-photon sources and detectors," *Review of Scientific Instruments*, vol. 82, no. 7, 2011.
7. E. Knill, R. Laflamme, and G. J. Milburn, "A scheme for efficient quantum computation with linear optics," *Nature*, vol. 409, pp. 46-52, 2001.
8. P. Kok, W. J. Munro, K. Nemoto, T. C. Ralph, J. P. Dowling, and G. J. Milburn, "Linear optical quantum computing with photonic qubits," *Reviews of Modern Physics*, vol. 79, no. 1, pp. 135-174, 2007.
9. M. A. Noginov, H. Li, Y. A. Barnakov, D. Dryden, G. Nataraj, G. Zhu, et al, "Controlling spontaneous emission with metamaterials," *Optics Letters*, vol. 25, no. 11, pp. 1863-1865, 2010.
10. J. G. Rarity, J. Fulconis, J. Duligall, W. J. Wadsworth, and P. S. J. Russell, "Photonic crystal fiber source of correlated photon pairs," *Optics Express*, vol. 13, no. 2, pp. 534-544, 2005.
11. R. Dong, J. Heersink, J. F. Corney, P. D. Drummond, U. L. Andersen, and G. Leuchs, "Experimental evidence for Raman-induced limits to efficient squeezing in optical fibers," *Optics Letters*, vol. 33, no. 2, pp. 116-118, 2008.
12. G. P. Agrawal. *Nonlinear fiber optics*. 3rd ed. San Diego: Academic Press; 2001.
13. H. J. McGuinness, M. G. Raymer, C. J. McKinstrie, and S. Radic, "Quantum frequency translation of single-photon states in a photonic crystal fiber," *Phys Rev Lett*, vol. 105, no. 9, 2010.
14. P. J. Mosley, J. S. Lundeen, B. J. Smith, P. Wasylczyk, A. B. U'Ren, C. Silberhorn, et al, "Heralded generation of ultrafast single photons in pure quantum States," *Phys Rev Lett*, vol. 100, no. 13, 2008.
15. P. S. J. Russell, "Photonic-Crystal Fibers," *Journal of Lightwave Technology*, vol. 24, no. 12, pp. 4729-4749, 2006.
16. R. F. Cregan, B. J. Mangan, J. C. Knight, T. A. Birks, P. S. Russell, P. J. Roberts, et al, "Single-Mode Photonic Band Gap Guidance of Light in Air," *Science*, vol. 285, no. 5433, pp. 1537-1539, 1999.

17. M. Azhar, G. K. L. Wong, W. Chang, N. Y. Joly, and P. S. J. Russell, "Raman-free nonlinear optical effects in high pressure gas-filled hollow core PCF," *Optics Express*, vol. 21, no. 4, pp. 4405-4410, 2013.
18. K. E. Lynch-Klarup, E. D. Mondloch, M. R. Raymer, D. Arrestier, F. Gerome, and F. Benabid, "Supercritical xenon-filled hollow-core photonic bandgap fiber," *Optics Express*, vol. 21, no. 11, pp. 13726-13732, 2013.
19. O. H. Heckl, C. J. Saraceno, C. R. E. Baer, T. Südmeyer, Y. Y. Wang, Y. Cheng, et al, "Temporal pulse compression in a xenon-filled Kagome-type hollow-core photonic crystal fiber at high average power," *Optics Express*, vol. 19, no. 20, pp. 19142-19149, 2011.
20. M. A. Finger, T. S. Iskhakov, N. Y. Joly, M. V. Chekhova, and P. S. J. Russell, "Raman-Free, Noble-Gas-Filled Photonic-Crystal Fiber Source for Ultrafast, Very Bright Twin-Beam Squeezed Vacuum," *Physical Review Letters*, vol. 115, no. 14, 2015.
21. M. A. Finger, N. Y. Joly, P. S. J. Russell, and M. V. Chekhova, "Characterization and shaping of the time-frequency Schmidt mode spectrum of bright twin beams generated in gas-filled hollow-core photonic crystal fibers," *Physical Review A*, vol. 95, no. 5, 2017.
22. M. C. Phan Huy, A. Baron, S. Lebrun, R. Frey, and P. Delaye, "Characterization of self-phase modulation in liquid filled hollow core photonic bandgap fibers," *Journal of the Optical Society of America B*, vol. 27, no. 9, pp. 1886-1893, 2010.
23. A. R. Bhagwat and A. L. Gaeta, "Nonlinear optics in hollow-core photonic bandgap fibers," *Optics Express*, vol. 16, no. 7, pp. 5035-5047, 2008.
24. M. Barbier, I. Zaquine, and P. Delaye, "Spontaneous four-wave mixing in liquid-core fibers: towards fibered Raman-free correlated photon sources," *New Journal of Physics*, vol. 17, no. 5, 2015.
25. F. Couny, F. Benabid, and P. S. Light, "Large-pitch kagome-structured hollow-core photonic crystal fiber," *Optics Letters*, vol. 31, no. 24, pp. 3574-3576, 2006.
26. P. S. J. Russell, P. Holzer, W. Chang, A. Abdolvand, and J. C. Travers, "Hollow-core photonic crystal fibres for gas-based nonlinear optics," *Nat Photon*, vol. 8, no. 4, pp. 278-286, 2014.
27. G. Antonopoulos, F. Benabid, T. A. Birks, D. M. Bird, J. C. Knight, and P. S. J. Russell, "Experimental demonstration of the frequency shift of bandgaps in photonic crystal fibers due to refractive index scaling," *Optics Express*, vol. 14, no. 7, pp. 3000-3006, 2006.
28. R. W. Boyd, *Nonlinear Optics*, 3rd ed. Burlington, Elsevier Science, 2008.
29. D. J. Griffiths, *Introduction to electrodynamics*. 3rd ed. Upper Saddle River, Prentice Hall, 1999.
30. R. Q. Twiss and R. H. Brown, "The Question of Correlation between Photons in Coherent Beams of Light," *Nature*, vol. 179, no. 4570, pp. 1128-1129, 1957.
31. L. J. Wang, C. K. Hong, and S. R. Friberg. "Generation of correlated photons via four-wave mixing in optical fibres," *Journal of Optics B: Quantum and Semiclassical Optics*, vol. 3, pp. 346-352, 2001.
32. M. Beck, *Quantum mechanics: theory and experiment*, New York, Oxford University Press, 2012.
33. A. Zeilinger, "Light for the quantum. Entangled photons and their applications: a very personal story," *Physica Scripta*, vol. 92 no. 7, 2017.

34. P. Yeh, A. Yariv, and C-S. Hong, "Electromagnetic propagation in periodic stratified media. I. General theory*," *Journal of the Optical Society of America*, vol. 67, no. 4, pp. 423-438, 1977.
35. P. Yeh, A. Yariv, and E. Marom, "Theory of Bragg fiber*," *Journal of the Optical Society of America*, vol. 68, no. 9, pp. 1196-1201, 1978.
36. P. Yeh and A. Yariv, "Bragg reflection waveguides," *Optics Communications*, vol. 19, no. 3, pp. 427-430, 1976.
37. F. Benabid, "Hollow-core photonic bandgap fibre: new light guidance for new science and technology," *Philos Trans A Math Phys Eng Sci*, vol. 364, no. 1849, pp. 3439-3462, 2006.
38. F. Benabid and P. J. Roberts, "Linear and nonlinear optical properties of hollow core photonic crystal fiber," *Journal of Modern Optics*, vol. 58, no. 2, pp. 87-124, 2011.
39. J. C. Travers, W. Chang, J. Nold, N. Y. Joly, and P. St. J. Russell, "Ultrafast nonlinear optics in gas-filled hollow-core photonic crystal fibers," *Journal of the Optical Society of America B*, vol. 28, no. 12, pp. 11-26, 2011.
40. F. Benabid, P. J. Roberts, F. Couny, P. S. Light, "Light and gas confinement in hollow-core photonic crystal fibre based photonic microcells," *Journal of the European Optical Society - Rapid publications*, vol. 4, 2009.
41. J. D. Joannopoulos, *Photonic crystals: molding the flow of light*, 2nd ed. Princeton, Princeton University Press, 2008.
42. N. M. Litchinitser, S. C. Dunn, P. E. Steinvurzel, B. J. Eggleton, T. P. White, R. C. McPhedran, et al. "Application of an ARROW model for designing tunable photonic devices," *Optics Express*, vol. 12, no. 8, pp. 1540-1550, 2004.
43. H. Ibach and H. Lüth, *Solid-state physics: an introduction to principles of materials science*, 4th ed. New York, Springer, 2009.
44. T. A. Birks, D. M. Bird, T. D. Hedley, J. M. Pottage, and P. S. J. Russell, "Scaling laws and vector effects in bandgap-guiding fibres," *Optics Express*, vol. 12, no. 1, pp. 69-74, 2004.
45. J. M. Pottage, D. M. Bird, T. D. Hedley, T. A. Birks, J. C. Knight, P. S. J. Russell, et al, "Robust photonic band gaps for hollow core guidance in PCF made from high index glass," *Optics Express*, vol. 11, no. 22, pp. 2854-2861, 2003.
46. N. Y. Joly, J. Nold, W. Chang, P. Hölzer, A. Nazarkin, G. K. Wong, et al, "Bright spatially coherent wavelength-tunable deep-UV laser source using an Ar-filled photonic crystal fiber," *Phys Rev Lett*, vol. 106, no. 20, 2011.
47. F. Tani, J. C. Travers, K. F. Mak, W. Chang, and P. Russell, "Modulation Instability in Xenon-Filled Hollow-Core Photonic Crystal Fiber," *Advanced Photonics Congress*, 2012.
48. J. Nold, P. Hölzer, N. Y. Joly, G. K. L. Wong, A. Nazarkin, A. Podlipensky, et al, "Pressure-controlled phase matching to third harmonic in Ar-filled hollow-core photonic crystal fiber," *Optics Letters*, vol. 35, no. 17, pp. 2922-2924, 2010.
49. S. O. Konorov, A. B. Fedotov, and A. M. Zheltikov, "Enhanced four-wave mixing in a hollow-core photonic-crystal fiber," *Optics Letters*, vol. 28, no. 16, pp. 1448-1450, 2003.
50. G. Bouwmans, F. Luan, J. C. Knight, P. S. J. Russell, L. Farr, B. J. Mangan, et al, "Properties of a hollow-core photonic bandgap fiber at 850 nm wavelength," *Optics Express*, vol. 11, no. 14, pp. 1613-1620, 2003.

51. D. G. Ouzounov, F. R. Ahmad, D. Müller, N. Venkataraman, M. T. Gallagher, M. G. Thomas, et al, "Generation of megawatt optical solitons in hollow-core photonic band-gap fibers," *Science*, vol. 301, no. 5640, pp. 1702-1704, 2003.
52. J. M. Fini, J. W. Nicholson, B. Mangan, L. Meng, R. S. Windeler, E. M. Monberg, et al, "Polarization maintaining single-mode low-loss hollow-core fibres," *Nature Communications*, vol. 5, no. 5085, 2014.
53. J. A. West, C. M. Smith, N. F. Borrelli, D. C. Allan, and K. W. Koch, "Surface modes in air-core photonic band-gap fibers," *Optics Express*, vol. 12, no. 8, pp. 1485-1496, 2004.
54. R. Amezcua Correa, F. Gerome, S. G. Leon-Saval, N. G. Broderick, T. A. Birks, and J. C. Knight, "Control of Surface Modes in Low Loss Hollow-Core Photonic Bandgap Fibers," Conference on Lasers and Electro-Optics/Quantum Electronics and Laser Science Conference and Photonic Applications Systems Technologies, 2008.
55. D. Milam, "Review and assessment of measured values of the nonlinear refractive-index coefficient of fused silica," *Applied Optics*, vol. 37, no. 3, pp. 546-550, 1998.
56. F. Benabid, J. C. Knight, G. Antonopoulos, and P. S. Russell, "Stimulated Raman scattering in hydrogen-filled hollow-core photonic crystal fiber," *Science*, vol. 298, no. 5592, pp. 399-402, 2002.
57. X. Li, J. Chen, P. Voss, J. Sharping, and P. Kumar, "All-fiber photon-pair source for quantum communications: Improved generation of correlated photons," *Optics Express*, vol. 12, no. 16, pp. 3737-3744, 2004.
58. H. J. Lehmeier, W. Leupacher, and A. Penzkofer, "Nonresonant third order hyperpolarizability of rare gases and N₂ determined by third harmonic generation," *Optics Communications*, vol. 56, no. 1, pp. 67-72, 1985.
59. E. W. Lemmon, M. O. McLinden, and D. G. Friend. "Thermophysical properties of fluid systems," *NIST Chemistry WebBook, SRD 69*, 2009.
60. A. Hitachi, V. Chepel, M. I. Lopes, and V. N. Solovov, "New approach to the calculation of the refractive index of liquid and solid xenon," *The Journal of Chemical Physics*, vol. 123, no. 23, 2005.
61. L. B. Railsback, *Some Fundamentals of Mineralogy and Geochemistry*, 2017. Available from: <http://www.gly.uga.edu/railsback/FundamentalsIndex.html>.
62. M. A. Weinberge and W. G. Schneider, "On the liquid-vapor coexistence curve of xenon in the region of the critical temperature," *Canadian Journal of Chemistry*, vol. 30, no. 5, pp. 422-437, 1952.
63. W. G. Pollard and R. D. Present, "On Gaseous Self-Diffusion in Long Capillary Tubes," *Physical Review*, vol. 73, no. 7, pp. 762-774, 1948.
64. B. S. Massey, *Mechanics of fluids*, 3d ed. New York: Van Nostrand Reinhold Co.; 1975.
65. C. A. Klein, "Characteristic strength, Weibull modulus, and failure probability of fused silica glass," *Optical Engineering*, vol. 48, no. 11, 2009.
66. J. R. Rogers and M. D. Hopler, "Conversion of group refractive index to phase refractive index," *Journal of the Optical Society of America A*, vol. 5, no. 10, pp. 1595-1600, 1988.